Chandra X-ray Studies of the Supernova Remnants G292.0+1.8 and G292.2–0.5 Containing the Young Pulsars J1124–5916 and J1119–6127

by

Marjorie Emily Gonzalez

A Thesis
Submitted to the Faculty of Graduate Studies
In Partial Fulfillment of the Requirements for the Degree of

MASTER OF SCIENCE

Department of Physics and Astronomy
University of Manitoba
Winnipeg, Manitoba

THE UNIVERSITY OF MANITOBA

FACULTY OF GRADUATE STUDIES

*****

COPYRIGHT PERMISSION PAGE

Chandra X-ray Studies of the
Supernova Remnants G292.0+1.8
and G292.2-0.5 Containing the Young
Pulsars J1124-5916 and J1119-6127

BY

Marjorie Emily Gonzalez

A Thesis/Practicum submitted to the Faculty of Graduate Studies of The University

of Manitoba in partial fulfillment of the requirements of the degree

of

Master of Science

A mis padres, mis hermanos y toda mi familia

"Yo digo que las estrellas le dan gracias a la noche
Porque encima de otro coche, no pueden lucir tan bellas..."
Silvio Rodriguez (1975) – "Yo digo que las estrellas"

To my parents, my brothers and all my family

"I think that the stars thank the night,
Because upon no other carriage could they look so beautiful..."
Silvio Rodriguez (1975) – "I think that the stars"

Acknowledgements

Many thanks to Dr. Samar Safi-Harb for her guidance, encouragement, patience, motivation and all those other things that made this work possible. Her dedication to the field and enthusiasm for the research have inspired me from the start and have helped me find an area of work that challenges me and captures my imagination. This project proved to be an incredible learning experience that would not have been as enriching without her as an advisor, for that I am very grateful.

I would also like to thank Dr. Richard Bochonko, whose lectures introduced me to the wonders of Astronomy. Choosing his first year class as back-up from an unavailable Anthropology class has been the best "substitute" of my academic career. Also, many thanks to Ian Cameron for his patience with my memory and to the other members of the Physics and Astronomy Department for putting up with me all these years. In addition, I would like to acknowledge the support given to me by NSERC during the course of my degree, it was much appreciated.

Special thanks to all my friends and fellow students for helping me keep my sanity, I would not have survived without the late night chats and recreational activities outside the department. I also take this opportunity to officially apologize for all the noise during lectures, labs and any other times (this goes to the professors too). You won't need the sound-proof rooms now.

Finally, I would like to give my deepest thanks and gratitude to my parents for giving me their love and support every day. I know all the difficult decisions and sacrifices you have had to make for us and I thank you for them. I would not be here, or be the person I am,

without you. Gracias de todo corazón, espero pagarles un día, y este trabajo es para ustedes, Edgar, Fernando y toda la familia.

Abstract

This thesis presents spectral and imaging X-ray studies of the Galactic supernova remnants (SNRs) G292.0+1.8 and G292.2–0.5 performed with the state-of-the-art *Chandra X-ray Observatory*. The analysis performed on G292.0+1.8 represents the first detailed spatially resolved spectroscopic study of this composite-type SNR, and the analysis of G292.2–0.5 represents the first high-resolution X-ray study of this young remnant and its associated high-magnetic field pulsar.

Spectral and imaging analysis of the remnant G292.0+1.8, containing the 135 ms pulsar (PSR) J1124–5916, were performed. The supernova blast wave and ejecta were identified by fitting the X-ray data with nonequilibrium ionization (NEI) models. A progenitor mass of 30–40 $M_{\odot}$ was derived by comparing the derived abundances from the NEI fits with those predicted from nucleosynthesis models. The intrinsic parameters of the supernova explosion such as its energy, age of the SNR, blast wave velocity and swept-up mass were derived using the Sedov interpretation. The estimated age of the remnant of $2,600^{+250}_{-200}$ yrs is close to the characteristic age of the pulsar of 2,900 yrs. The properties of the pulsar wind nebula (PWN) surrounding PSR J1124–5916 were also derived in light of the Kennel & Coroniti model. In addition, the first evidence for a steepening of the PWN power law index with increasing radius was found, as expected from synchrotron losses.

The *Chandra* observation of the remnant G292.2–0.5 allowed for the detection of the X-ray counterpart of its associated high-magnetic field radio pulsar J1119–6127. A faint 3″x6″ extended component surrounding the pulsar was identified at energies above ~1.2 keV,

representing the first evidence for a PWN. The combined emission from the pulsar and its PWN was well described by a power law with a photon index $\Gamma = 2.2^{+0.6}_{-0.3}$ and unabsorbed 0.5–10 keV luminosity of $\left(5.5^{+10}_{-3.3}\right)\times 10^{32}$ ergs s^{-1} at a distance of 6 kpc. The emission from the interior of the SNR was well described by either a single NEI model with a high temperature (kT > 15 keV) or a two-component NEI plus power law model with a flat photon index (kT ~ 1.5 keV and Γ ~ 1.1).

The study of these two systems demonstrates the power of spatially resolved X-ray spectroscopy in finding new PSR/SNR associations and in resolving the thermal and nonthermal emission associated with SNRs, pulsars and their nebulae.

Table of Contents

List of Figures

List of Tables

Motivation

The study of supernova explosions and supernova remnants (SNRs) helps us in understanding the chemical evolution of the universe. They aid both in the production of elements during the explosion, and their dispersion into the interstellar medium (ISM). Therefore, they also represent the principal contributor to the chemical evolution of galaxies. A type II supernova explosion is the energetic explosive event that occurs at the end of a massive star's life. The stellar core collapses due to gravity and blows off its outer layers, releasing a kinematic energy of $\sim 10^{51}$ ergs which energizes the surrounding ISM. The explosion sends a shock wave that expands through the ISM and the ejected material during the event (ejecta). At the boundary between the ISM and ejecta, both a forward and reverse shocks are produced. Thus, two nested shock-wave shells appear, both expanding with time and creating an observable supernova remnant. These relics of the explosion last for a long time and can be observed at various wavelengths, such as radio, optical and X-rays. Another mechanism that can produce a supernova explosion is the disruption of a white dwarf star in a binary system (a type Ia supernova explosion). However, this thesis will only deal with those explosions that leave behind a collapsed core and a SNR.

One of the possible outcomes of a type II explosion is a high density, rapidly rotating neutron star, which may manifest itself as a pulsar (PSR) directly or through its interaction with its surroundings. As the neutron star rotates, it loses energy as it slows down and forms a relativistic hot bubble around the pulsar referred to as a pulsar wind nebula (PWN, see Section 2.3) that manifests itself through synchrotron radiation from radio to X-ray energies.

This thesis deals with the studies of two galactic supernova remnants at X-ray wavelengths, G292.0+1.8 and G292.2-0.5. Spectral and spatial data obtained with the *Chandra X-ray Observatory* are used to carry out this analysis. The main goal is to study the properties of the remnants (and their associated neutron stars) in X-rays and to derive their basic physical parameters. Chapter 1 is an overview of SNRs, their classification and evolution. Chapter 2 presents a summary of the fundamental pulsar and PWNe characteristics. Chapter 3 reviews the dominant emission mechanisms of these objects at X-ray wavelengths and the physical properties that can be derived from them. Chapter 4 consists of an overview of the capabilities offered by *Chandra* and a review of the data reduction issues taken into account for this thesis. Chapters 5 and 6 present the analysis and results obtained for G292.0+1.8 and G292.2–0.5, respectively. Finally, Chapter 7 presents the conclusions drawn for this work.

Chapter 1

Review of Supernova Remnants

1.1 Classification of Supernova Remnants

Supernova remnants (SNRs) can be observed from radio to X-ray frequencies. Their classification is based on their morphology and they are divided into "shells", "plerions" and "composites". Green (2001) catalogues 231 Galactic SNRs, of which 153 are shells, 8 are plerions, 18 are composites and 52 are unclassified.

1.1.1 Shell-type remnants

Shell-type remnants are characterized by their limb-brightened morphology in the radio and X-rays. The morphology of these objects is a roughly spherical shell. Typical examples include Cassiopeia A (G111.7-2.1), Tycho's remnant (G120.1+1.4) and Kepler (G4.5+6.8). Figure 1.1 shows the *Chandra* high-resolution X-ray image of the SNR Cassiopeia A.

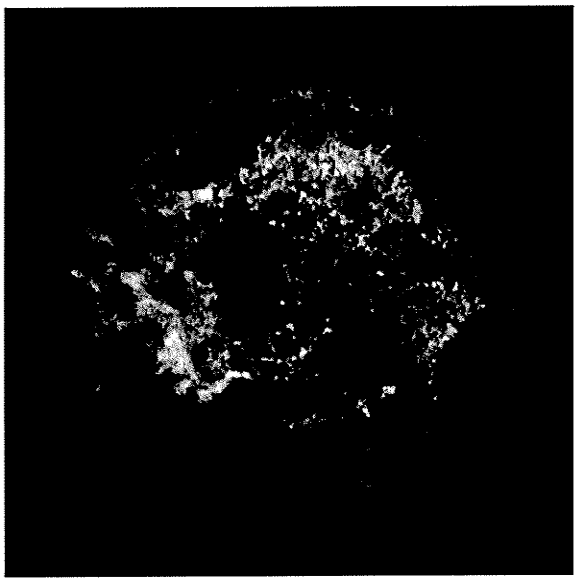

Figure 1.1: X-ray image of shell-type remnant Cassiopeia A. Credit: NASA/CXC/SAO. Available at http://chandra.harvard.edu/photo/0237/index.html.

At radio wavelengths, the emission from shell remnants is polarized, with a nonthermal spectrum that can be characterized by a single power law, spectral flux density $S_\nu \propto \nu^{-\alpha}$ with a spectra index of α, over several orders of magnitude (see Section 3.4). The power law spectral index varies from α ~0.6 for young remnants, to α ~0.5 for the older ones. This nonthermal emission is due to synchrotron radiation from relativistic electrons gyrating around the magnetic field lines in the shells of the SNRs.

At X-ray wavelengths there is a strong thermal component. This emission arises from optically-thin plasma heated by the forward and reverse shock waves to temperatures of ~10^6–10^8 K. The radiation mechanisms responsible for this emission are thermal bremsstrahlung and line emission (see Section 3.3). The emitting material can be both

material ejected from the progenitor star and the swept-up interstellar gas. In young remnants (< 10^4 yrs), the emission is predominantly from shock-heated supernova ejecta. In older remnants, the temperature of the gas decreases and makes them harder to detect at X-ray wavelengths.

Recently, nonthermal X-ray emission has also been detected in shell-type remnants, being well described by a power law spectrum with photon index Γ ~2–3 (see Section 3.4). Examples include SN1006 (Koyama et al. 1995, Tanimori 1998) and G347.3-0.5 (Slane et al. 1999). This has provided evidence for particle acceleration up to energies of <100 TeV by a strong shock wave.

1.1.2 Plerionic-type remnants

A "plerion" is a centrally-filled remnant, also called "Crab-like" since the emission arises mostly from the central nebula associated with the neutron star, as in the Crab nebula. The pulsar converts a significant fraction of its spindown energy into a pulsar wind, believed to be relativistic with a Lorentz factor of ~10^5–10^6. The kinetic energy of this wind is converted into relativistic hot plasma at a termination shock (see Section 2.3). This produces the nonthermal emission characteristic of a plerion in the form of a pulsar wind nebula (PWN). At radio and X-ray frequencies, the emission is due to synchrotron radiation from electrons supplied by the neutron star or its PWN, not the remnant itself. The spectrum is described by a power law, with a flat index of α ~0–0.3 at radio energies, steepening to α ~0.5–1.5 in X-rays. Figure 1.2 shows an image of the Crab nebula, the classical model for this SNR type.

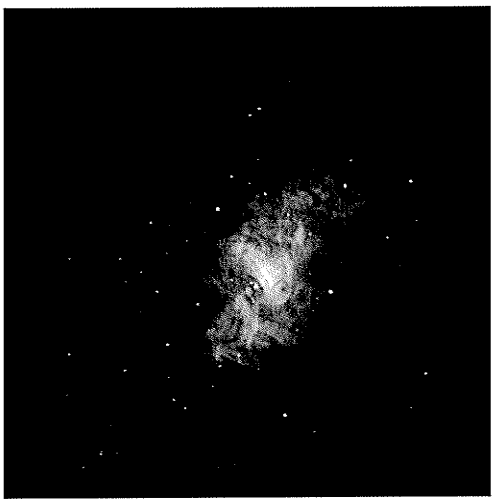

Figure 1.2: A combined image of the Crab Nebula showing X-rays in blue, optical in green, and radio in red colors. Credits: X-ray: NASA/CXC/ASU/J. Hester et al.; Optical: NASA/HST/ASU/J. Hester et al.; Radio: VLA/NRAO. Available at http://chandra.harvard.edu/photo/2002/0052/more.html.

In general, pulsars are believed to have a proper motion with respect to the original site of the supernova explosion. In turn, they will not always be located at the center of the SNR or at the brightest part of the SNR. At radio wavelengths, due to the large synchrotron lifetime of the electrons, the region where the pulsar deposited most of its rotational energy will still have the largest surface brightness. However, at X-ray wavelengths, the synchrotron lifetime is shorter and the brightest spot will mark the current position of the pulsar. Therefore, observations of plerions give an indication of the location of the pulsar's position in the SNR, even when the pulsar itself has not been detected.

1.1.3 Composite remnants

In composite remnants both the shell and the plerion are present. The study of composite remnants is of interest since both the compact object and the ejected material from the supernova explosion can be studied independently. This thesis will concentrate on high resolution, X-ray studies of two young remnants of this type, G292.0+1.8 and G292.2-0.5. Figure 1.3 shows the X-ray image of the composite remnant G292.0+1.8, where the emission from the SNR is constrained to red and green colors while the emission from the pulsar and its PWN is shown in blue (see Section 5.3).

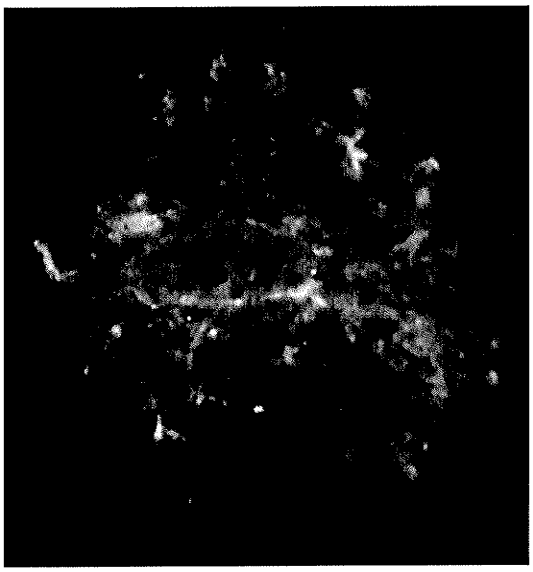

Figure 1.3: 0.5-10.0 keV X-ray image of composite remnant G292.0+1.8 (MSH 11-54) obtained with the Chandra Observatory.

1.2 Evolution of SNRs

The evolution SNRs is generally divided into four phases: free expansion phase, adiabatic

(or Sedov) phase, radiative phase and disappearance phase (Woltjer 1972). For simplicity, it is assumed that the evolution occurs in a uniform ISM. In the following, the evolution of the overall SNR is considered; the evolution of a PWN (if one is present, which in turn influences the SNR's classification) is discussed in detail by van der Swaluw (2003) and van der Swaluw et al. (2001).

1.2.1 Free expansion phase

The supernova explosion generates a shock wave that first propagates through the outer layers of the progenitor star. The free expansion phase starts when this shock wave reaches the edge of the atmosphere of the star. The ejecta then expand rapidly and sweep up the ambient ISM. Since the X-ray emission in this stage is dominated by ejecta, X-ray spectra at this stage give us information on the chemical composition of heavy elements produced during the supernova explosion. In this expanding stage, almost all the mechanical energy of the SNR is converted into kinetic energy. Since the mass from the ejecta is still much larger than the swept-up mass from the ISM, the result is an almost constant expansion velocity determined by the initial kinetic energy, E_0. The expansion then proceeds according to

$$R_{snr} = \upsilon_{snr} t \; ; \; \upsilon_{snr} \approx \sqrt{\frac{2E_0}{M_{ej}}} \tag{1.1}$$

where R_{snr} and υ_{snr} are the SNR's radius and expansion velocity, respectively, t is the age

of the remnant and M_{ej} is the mass of the ejecta. Figure 1.4 shows an example of a remnant in this stage: an extremely young (~40 yrs-old) SNR detected in the starburst galaxy M82 (Pedlar et al. 2000).

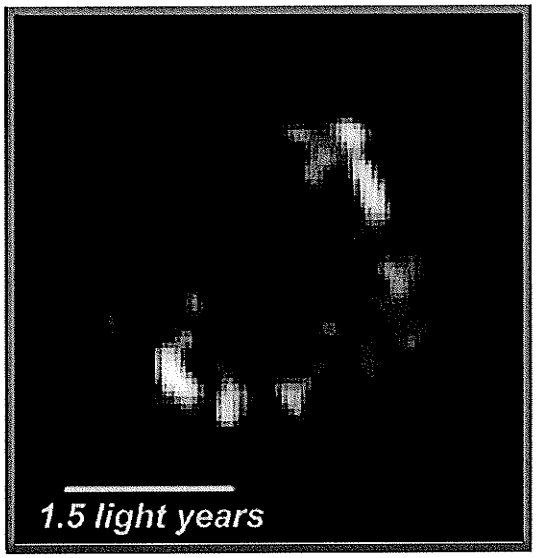

Figure 1.4: A young SNR in the free expansion phase in the galaxy M82. Adapted from http://antwrp.gsfc.nasa.gov/apod/ap991216.html.

1.2.2 Adiabatic (Sedov) stage

The transition to the adiabatic stage occurs when the mass of the swept-up material exceeds ~10 times the mass of the ejecta, M_{ej}. Energy losses due to radiation are still negligible compared to the original explosion energy, E_0, and the remnant expands adiabatically. In the transition to this stage, the blast wave gradually decelerates and causes

another shock wave to propagate inward through ejecta, called the reverse shock, which heats the interior of the remnant (McKee 1974). An example of a SNR in this stage is Cas A (see Figure 1.1).

In this adiabatic stage, the evolution of the SNR can be approximately described as that of a shock wave generated by a point explosion propagating in a uniform medium. In the case of an ideal gas, the shock wave is described by differential equations describing the conservation of mass, momentum and energy. This phase is also called the *Sedov phase* after L. I. Sedov, who in 1959 showed that the conservation equations can be simplified by making the assumption of a *similarity solution*, where fluid quantities depend on three independent variables: the age of the remnant, t, initial explosion energy, E_0 and the ambient density, ρ_0. The similarity variable, ξ, combines these parameters in the following dimensionless expression:

$$\xi = r\left(\frac{\rho_0}{E_0 t^2}\right)^{1/5} \tag{1.2}$$

Setting the outer blast wave at a specific value, $\xi = \xi_0$, the radius and expansion velocity of the SNR are given by

$$R_{snr} = \xi_0\left(\frac{E_0 t^2}{\rho_0}\right)^{1/5} \tag{1.3}$$

$$\upsilon_{snr} = \frac{dR_{snr}(t)}{dt} = \frac{2}{5}\frac{R_{snr}}{t} \tag{1.4}$$

where ξ_0 can be determined from energy conservation. One then finds that $\xi_0 \approx 1.1516$ for an ideal monatomic gas with specific-heat ratio $\gamma(=C_P/C_V)=5/3$ (Sedov 1959).

1.2.3 Radiative phase

The Sedov solution is a quite accurate approximation as long as cooling due to radiation losses can be neglected and the total energy is conserved. A transition takes place when radiation losses become important in the shell of the swept-up material and the temperature behind the shock drops to ~10^6 K. The expansion of the remnant is no longer adiabatic. Since the pressure in the outer shell becomes lower as the temperature decreases, the swept-up mass collapses into a thin, dense layer and cools rapidly. However, the interior of the SNR still expands adiabatically. Thus, the shell expands by the pressure of the interior gas with PV^{γ} = constant, where P and V are the mean pressure and volume of the interior gas, respectively, and $\gamma(=C_P/C_V)$ is the specific-heat ratio. With $P \propto \upsilon_{snr}^2$, $V \propto R_{snr}^3$, and $\gamma = 5/3$, the SNR expands as

$$R_{snr} \propto t^{2/7} \tag{1.5}$$

This stage is also called the "pressure-driven snowplow phase" since the interior pressure pushes the thin shell through the ISM, as a snowplow would (McKee & Ostriker 1977). The next stage marks the beginning of the end of the SNR when the pressure in the interior becomes comparable to the pressure of the ISM as the interior cools. There will be no force acting on the shell of the SNR, so momentum is conserved. Thus, this stage is also called

the "momentum-conserving snowplow stage". The shock continues to sweep up the interstellar gas with the equation, $M_s \upsilon_{snr}$ = constant, where M_s is the mass of the shell. With $M_s \propto R_{snr}^3$, this becomes

$$R_{snr} \propto t^{1/4} \tag{1.6}$$

Figure 1.5 shows the X-ray image obtained with the *Einstein* observatory of the Cygnus Loop, an example of a SNR where certain regions exhibit signs of having entered the radiative phase (Blondin et al. 1998).

Figure 1.5: Einstein X-ray image of the Cygnus Loop SNR. Adapted from http://www.seds.org/pub/images/deepspace/einstein-cygnus-loop.gif

1.2.4 Disappearance phase

After the shock velocity drops to the sound speed of the ISM, the shock wave disappears

and the expansion velocity is comparable to the random motion of the ISM. The remnant becomes fainter and indistinguishable from the surrounding medium, merging into the ISM and leaving behind a cavity with higher temperature than the surroundings. The event of merging has been estimated to take place ~750,000 years after the supernova explosion (Cioffi 1990).

Chapter 2

Review of Pulsars and Pulsar Wind Nebulae

2.1 Introduction

One of the main purposes of this thesis is to study the X-ray properties of the pulsars associated with the two Galactic SNRs G292.0+1.8 and G292.2-0.5. Thus, three essential pulsar quantities are derived below: the spindown luminosity, magnetic field strength and the characteristic age, all as a function of the pulsar's period, P, and period derivative, $\dot{P}$, two of the most basic pulsar characteristics. Observations of pulsars at high energies are also discussed, as well as the basic characteristics of pulsar wind nebulae.

2.2 Pulsar Characteristics

2.2.1 Spindown luminosity

The total energy of a system is one of its most fundamental properties. In the case of "ordinary" radio pulsars, rotational kinetic energy is thought to be the source of the observed pulsed radiation as well as the power source that drives the possible synchrotron nebula surrounding it. These are referred to as rotation-powered pulsars. Taking the derivative with respect to time of the kinetic energy, E, of a rotating body with moment of inertia, I, and rotation frequency, Ω,

$$\frac{d}{dt}(E) = \frac{d}{dt}\left(\frac{1}{2} I\Omega^2\right) \tag{2.1}$$

and expressing in terms of the period, P, and period derivative, $\dot{P}$,

$$P = 2\pi\left(\frac{1}{\Omega}\right) \; ; \; \dot{P} = -2\pi\left(\frac{\dot{\Omega}}{\Omega^2}\right) \tag{2.2}$$

the expression for the *spin-down luminosity,* $\dot{E}$, then becomes

$$\dot{E} = -4\pi^2 I \frac{\dot{P}}{P^3} \tag{2.3}$$

(Carroll & Ostlie 1996). For typical neutron star parameters (radius of 10 km and mass of $1.4M_{\odot}$) and assuming that the neutron star is a rigid sphere, the moment of inertia is $I = 10^{45}\ g\ cm^2$.

2.2.2 Magnetic field strength

Rotation-powered pulsars have been observed to spin-down, that is, their spin period P increases and thus they have a positive period derivative, $\dot{P}$. This is thought to be a result of magnetic dipole braking. This phenomenon gives rise to the same radiation that results from a rotating magnetic dipole. From classical electrodynamics, the power, P_{ν}, radiated from a magnetic dipole, $\vec{m}$, is given by

$$P_v = \frac{2}{3c^2}\left|\ddot{m}^2\right| \tag{2.4}$$

A neutron star with surface dipole field strength, B, and radius, R, has an associated magnetic dipole moment $|\vec{m}| = BR^3$. If the magnetic and rotation axis are separated by an angle α, equation (2.4) becomes

$$P_v = \frac{2B^2R^6\Omega^4 \sin^2\alpha}{3c^3} \tag{2.5}$$

Equating this with equation (2.3) for $\dot{E}$ and assuming that $\sin\alpha = 1$ (for maximum amount of braking and lower limit on B) the *surface magnetic dipole field* is given by (Manchester & Taylor 1977),

$$B = \left(\frac{3\,I\,c^3 P\dot{P}}{8\pi^2 R^6}\right)^{1/2} = 3.2\times10^{19}\left(P\dot{P}\right)^{1/2}\ G \tag{2.6}$$

2.2.3 Characteristic age

The age of a pulsar, τ, can be estimated by starting with the assumption that it slows down at a rate that is proportional to the rotation frequency, raised to the power n, called the *braking index*, as follows

$$\dot{\Omega} \equiv -k\Omega^n \tag{2.7}$$

After taking an additional derivative with respect to time, the braking index is given by

$$n = \frac{\Omega\ddot{\Omega}}{\dot{\Omega}^2} \tag{2.8}$$

Now, integrating Equation (2.7) gives

$$\frac{d\Omega}{dt} = -k\Omega^n$$

$$\frac{\Omega^{(-n+1)}}{(-n+1)}\bigg|_{\Omega_0}^{\Omega} = -kt'\Big|_{t'=0}^{t'=\tau}$$

$$\tau = \frac{\Omega^n}{\dot{\Omega}}\left(\frac{\Omega^{(-n+1)} - \Omega_0^{(-n+1)}}{-n+1}\right)$$

$$\tau = \frac{1}{(n-1)}\frac{P}{\dot{P}}\left[1 - \left(\frac{P_0}{P}\right)^{n-1}\right] \tag{2.9}$$

Furthermore, if the pulsar slows down due to magnetic dipole braking, the above equations for $\dot{E}$ and B can be used to show that $\dot{\Omega} \propto \Omega^3$, or that the braking index in this case is $n = 3$. In most cases, it is assumed that $P >> P_0$ and equation (2.9) reduces to the *characteristic age* expression

$$\tau_c = \frac{P}{2\dot{P}} \tag{2.10}$$

(Manchester & Taylor 1977). This can then be used as an approximation for the age of the pulsar.

2.2.4 High energy observations

X-ray observations of rotation-powered pulsars provide a powerful diagnostic tool to study their energetics and emission mechanisms. Although they have traditionally been more easily studied at radio wavelengths, only a small fraction ($\sim 10^{-7}$–10^{-5}) of the spindown luminosity, $\dot{E}$, is released as radio pulsations. It is believed that a significant fraction of the spin-down power emerges as a relativistic wind of particles and magnetic fields. When this wind is confined by the surrounding medium, an observable synchrotron nebula or pulsar wind nebula (PWN) is produced. In X-rays, the PWN detected around the Crab pulsar provides the prototype for this phenomenon (see Figure 2.1). Studies of the morphology and spectrum of PWNe are important in determining the content and energy spectrum of the wind, probing the conditions of the ambient medium (SNR or ISM) and understanding the shock acceleration mechanism (e.g. Gaensler et al. 2002, Helfand et al. 2001).

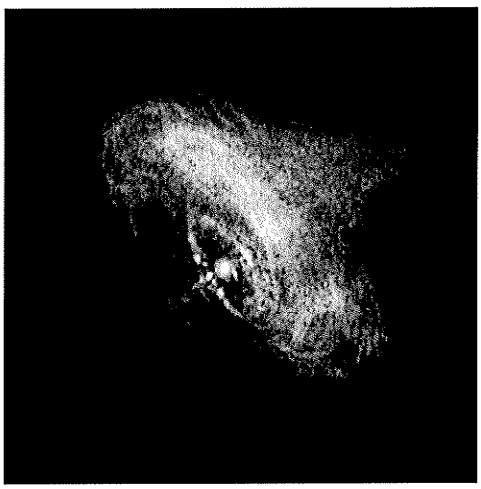

Figure 2.1: 0.3-3.0 keV X-ray image of the PWN surrounding the Crab pulsar obtained with the Chandra Observatory. Credit: NASA/CXC/SAO/Hester et al. Available at http://chandra.harvard.edu/photo/2002/0052/more.html

X-ray observations of pulsars are also important in searching for the remnant of the supernova explosion if one is not known previously. Studies of the remnants are useful for numerous reasons, including measurement of the elemental abundances of the progenitor star and determining the shock conditions in the SNR through spectral analysis. In addition, associations between SNRs and pulsars can provide independent measurements for the distance and age of the system.

2.3 PWN characteristics

Our basic understanding of "Crab-like" PWNe arises from the model presented by Rees and Gunn (1974) and extended by Kennel and Coroniti (1984a, b). In this model, a relativistic wind is injected from the pulsar into its surroundings. The confinement of the wind by the ejecta, the swept-up interstellar material, or the ram pressure of a fast moving pulsar creates a synchrotron bubble referred to as a pulsar wind nebula or plerion. A schematic of the PWN surrounding the Crab pulsar is shown in Figure 2.2.

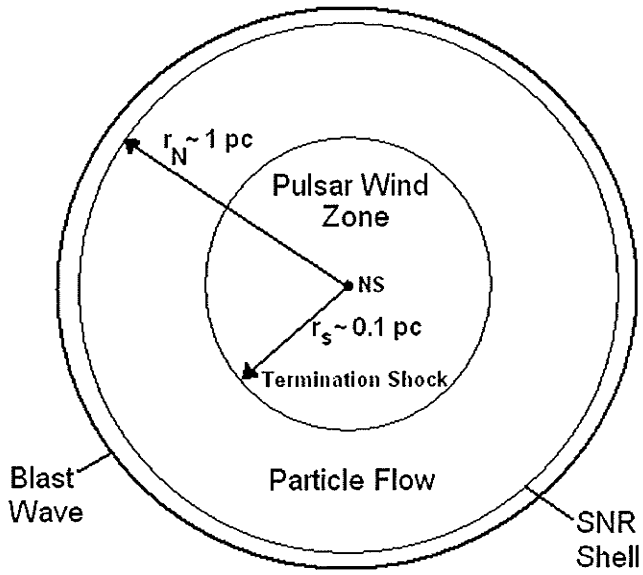

Figure 2.2: Schematic view of the Crab pulsar and its PWN, with r_s and r_n representing the shock radius and overall nebular radius, respectively (see below).

The pulsar wind, driven by the spindown energy, is terminated at a wind termination shock. Considering a constant mass injection, $\dot{M}$, by the pulsar wind, the density in the pulsar wind region, ρ_w, is given by mass conservation:

$$\rho_w = \frac{\dot{M}}{4\pi r^2 \upsilon_w} \tag{2.11}$$

Here, the velocity of the pulsar wind is noted by υ_w. Multiplying and dividing by a factor of υ_w gives the following expression for the shock radius, r_s:

$$r_s = \left(\frac{\dot{M}\upsilon_w}{4\pi\rho_w \upsilon_w^2} \right)^{1/2} \tag{2.12}$$

This equation is non-relativistic. Since the pulsar wind is relativistic (Lorentz bulk factor of 10^5–10^6) the above expression is converted by taking the limit $\upsilon_w \to c$ and multiplying the energy and momentum by a factor of c to approximate them to their associated relativistic counterparts, giving

$$r_s = \left(\frac{\dot{E}}{4\pi \rho_w \upsilon_w^2 c} \right)^{1/2} = \left(\frac{\dot{E}}{4\pi P_w c} \right)^{1/2} \tag{2.13}$$

where P_w is the pressure of the wind. The shock radius also marks the site at which the wind's ram pressure balances the total magnetic and particle pressure within the bulk of the nebular volume. Assuming equipartition between the particles and magnetic fields, the total nebular pressure is then given by

$$P_n = \frac{B_n^2}{4\pi} \tag{2.14}$$

where B_n is the nebular magnetic field. Then, equating $P_n = P_w$ can provide additional estimates of the PWN characteristics (see Section 5.5.3).

In addition, the pulsar wind is further characterized by its magnetization parameter, σ, representing the ratio of electromagnetic flux, $\upsilon B^2 / 4\pi$, to particle energy flux, $n\upsilon\gamma mc^2$. Here, n is the particle density and γmc^2 is the energy per particle, where $\gamma = 1/\sqrt{1-(\upsilon/c)^2}$ is the Lorentz factor. The magnetization parameter determines the efficiency of converting the energy contained by the pulsar wind into observable synchrotron radiation.

An estimation of the magnetization parameter can be made as follows (Kennel & Coroniti 1984a): we first take into account that conservation of magnetic flux requires that the strength of the field accumulated in the nebula increases linearly with radius ($B \propto r$) until the magnetic and particle pressures become comparable at the shock radius, r_s. In addition, the hydrodynamic particle flow is subsonic and must be nearly isobaric, its flow speed will then increase as r^2 with increasing radius ($\upsilon \propto r^2$) until it matches the expansion velocity of the nebula at r_n, the nebular radius. We can then make the approximation

$$\sigma \approx \left(\frac{r_s}{r_n} \right)^2 \qquad (2.15)$$

Equation (2.15) applies for low values of the magnetization parameter (σ<<1), or equivalently, for cases where the wind is particle- (as opposed to field-) dominated and a significant part of the wind luminosity is converted into synchrotron radiation (Kennel & Coroniti 1984a,b). For large values of the magnetization parameter (σ>>1), it can be shown that $\sigma \approx 36\pi P_n \gamma_n / B_n^2$ (Kennel & Coroniti 1984a), where P_n, γ_n and B_n are the nebular pressure, Lorentz factor and magnetic field, respectively.

Chapter 3

X-ray Radiation Mechanisms

3.1 Introduction

Supernova remnants produce intense radio and X-ray radiation for tens of thousands of years. In young remnants, the pulsar and its PWN can dominate the observed emission for a thousand years or more. At X-ray wavelengths, composite-type remnants contain thermal emission arising from shock-heated ejecta and the ISM. In addition, they contain nonthermal emission arising from PWNe. When characterizing the emission, the effects of interstellar absorption must also be taken into account. The following is a review of the main radiation mechanisms that come into play when analyzing the X-ray emission from composite-type SNRs.

3.2 Photoelectric absorption

In the photoelectric absorption process, an atom absorbs a photon and an electron is emitted. The energy of the emitted electron is given by the incident photon energy minus its binding energy. Since the X-ray photon is removed from the primary X-ray beam, this process contributes to the attenuation of the beam as shown schematically in Figure 3.1.

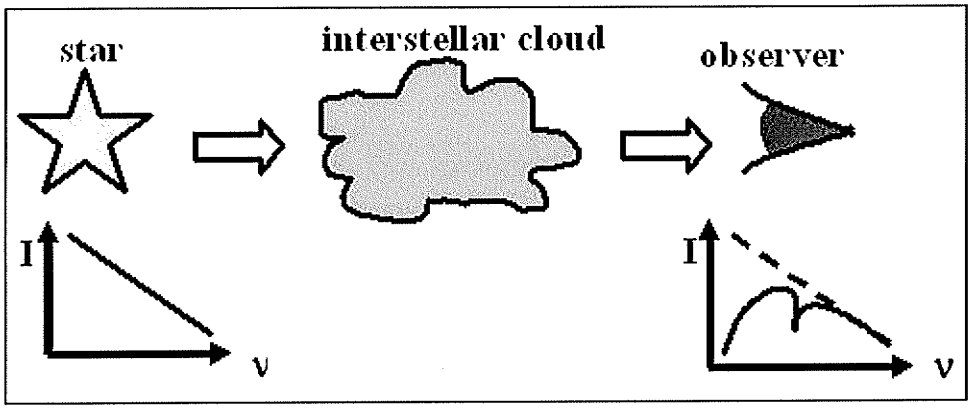

Figure 3.1: Schematic showing the absorption of soft X-ray photons by the ISM and its effect on the detected spectrum.

Column density is defined as the number of absorbing atoms per unit area along the line of sight to the background source that is being absorbed. The fraction of the original flux lost due to absorption is then given by

$$dF = -Fn_Z\sigma_Z(E)dl \tag{3.1}$$

where n_Z is the number density of the absorbing element Z, $\sigma_Z(E)$ is the cross section of element Z at energy E, and dl is the optical path length over which absorption takes place. Integrating over the path length gives the following expression for the observed source flux, F, in the presence of photoelectric absorption

$$F = F_0 e^{-\sigma_Z(E)\int n_Z dl} \tag{3.2}$$

The spectral analysis in this thesis takes into account the effects of interstellar absorption due to Hydrogen, with the Hydrogen column density given by (Gorenstein 1977),

$$N_H = \int n_H dl \ cm^{-2} \tag{3.3}$$

3.3 Thermal emission

The assumptions made when studying the thermal plasma in SNRs are that it represents: a) an optically-thin plasma in which collisional processes take place, b) a plasma with low density (~1 cm^{-3}) and high temperature (~10^6-10^8 K), and c) a plasma that has been heated instantaneously by the shock wave to a high temperature. Thermal contributions to the emission from SNRs arise mainly from gas in the ISM heated by the shock wave and from ejecta heated by the reverse shock. This thermal emission consists of both continuum and emission lines. Spectral analysis of this emission at X-ray wavelengths provides important physical parameters:

- The presence of emission lines allows for the determination of the plasma's chemical composition and the lines' relative strengths give a measure of their elemental abundances
- The energy shift of an emission line from its equilibrium value gives the degree of ionization of the plasma, and
- A measurement of the continuum emission allows for an estimate of the temperature of the plasma.

In addition, the emission from young SNRs in the Sedov phase can be used to estimate some of the remnant's basic physical parameters (see Section 3.3.2).

In optically-thin plasma, as is the case here, ionization processes such as collisional ionization dominate the production of thermal line emission. Especially in young SNRs, nonequilibrium ionization plays an important role and the thermal continuum emission arises mainly from thermal bremsstrahlung. The following is a summary of the above thermal processes.

3.3.1 Collisional ionization

Collisional ionization is the further ionization of an ion induced by the collision with an energetic electron (see Figure 3.2). On energetic grounds, it is usually the outermost electrons that are removed. Ionization by electron collisions is important if the gas temperature approaches a fraction of the ionization threshold temperature of the most abundant ions in the gas. Collisional ionization acts as a cooling mechanism since energy is lost from the electron sea to further ionize an ion.

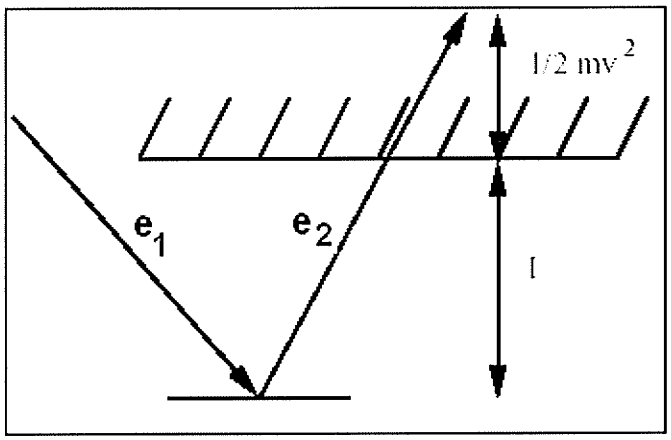

Figure 3.2: Schematic of collisional ionization.

The equation for this reaction is given by (Mewe 1999)

$$(Z,z)+e^{-}\rightarrow(Z,z+1)+e^{-}+e^{-} \tag{3.4}$$

The collisional ionization rate, $\gamma_{coll.}$, depends on the electron velocity distribution as follows

$$\gamma_{coll.}(z,z+1)=C_Z(z,T_e)n_e=\int_{\upsilon_{thresh}}^{\infty}\sigma_i(\upsilon)\upsilon f(\upsilon)d^3\upsilon=\langle\upsilon\sigma_i\rangle \tag{3.5}$$

where n_e is the electron number density, σ_i is the collisional ionization cross-section and C_Z is the collisional ionization rate coefficient (in units of cm^3 s). C_Z is typically presented in tabulated form with the fitting formula

$$C_Z(z,T)=A_Z T^{1/2}\frac{\exp(-I/kT)}{1+a_Z(T/T_Z)} \tag{3.6}$$

where $T_Z=I/kT$. For examples of C_Z values, see Arnaud & Rothenflug (1985) and Shull & van Steenburg (1982).

In an optically-thin plasma, the ionization state of the collisional plasma is said to be in *collisional ionization equilibrium* (CIE) if the atoms are ionized just to what would be expected from the plasma temperature, and thus, the ionization rate and recombination rate are balanced. The plasma is *underionized* (ionizing) if the atoms are less ionized and the ionization rate exceeds the recombination rate. This state has been observed in X-ray spectra of young SNRs (see below). The plasma is *overionized* (recombining) if the atoms are more highly ionized than would be expected if the plasma were in CIE and the recombination rate exceeds the ionization rate. This state has not been observed in X-ray spectra of SNRs.

If we define an "ionization temperature", kT_z, which represents the degree of ionization, when the atoms are ionized to what is expected in a CIE plasma with an electron temperature of kT_e', we have $kT_z = kT_e'$. The ionization state of the plasma is then expressed by the relation between kT_e and kT_z. In this way, $kT_z = kT_e$ means ionization equilibrium, $kT_z < kT_e$ means underionized, and $kT_z > kT_e$ means overionized.

3.3.2 Nonequilibrium ionization

The plasma in young SNRs is expected to be in *nonequilibrium ionization* (NEI) since the characteristic timescale for the electron temperature to be equal to the ion temperature is $\sim 1.5 \times 10^{11} n_0 t_{kyr}$ (in units of $s\ cm^{-3}$) in the case of a blast wave in the Sedov solution (see below), where n_0 is the Hydrogen ambient density (in cm^{-3}) and t_{kyr} is the age of the SNR in

units of 1,000 yrs (Masai 1994).

The collisional ionization rate equation for the element of atomic number Z can be written as

$$\frac{dn_z}{d(n_e t)} = S_{z-1} n_{z-1} - (S_z + \alpha_z) n_z + \alpha_{z+1} n_{z+1} \tag{3.7}$$

(Liedahl 1999), where n_z and n_e are the number densities of the ions with charge z and the number density of electrons, respectively. In addition, S_z represents the ionization rate coefficient of an ion from charge z to $z+1$, and α_z is the recombination rate coefficient of an ion of charge z to and $z-1$. In the equilibrium condition, we have $dn_z/d(n_e t) = 0$. The ionization timescale, τ, can be independently estimated from the zero-th order approximation to be (Masai 1994),

$$\tau = n_e t \approx \sum_{z=0}^{Z} (S_z + \alpha_z)^{-1} \approx \left[(S_z + \alpha_z)_{\min|S_z - \alpha_z|} \right]^{-1} \approx 10^{12}\ s\ cm^{-3} \tag{3.8}$$

where $(S_z + \alpha_z)_{\min|S_z - \alpha_z|}$ means the value of the element that gives the minimum difference between S_z and α_z (i.e. equilibrium between ionization and recombination). Thus, in these models the plasma is characterized by the electron temperature, kT_e, and the ionization timescale, $\tau = n_e t$.

The NEI condition of the plasma tells us how the SNR has evolved by comparing kT_z to kT_e, since kT_z gradually approaches kT_e on a remarkably long timescale of 10^{12-13} s (~10^4–

10^5 yrs). As the plasma approaches ionization equilibrium, two main effects are detected (Kaastra and Bleeker 1991): first, elements with higher atomic number become ionized at later times, creating a general shift of line complexes from low to high energies. Second, the effective line centroid for each element gradually shifts due to increasing ionization stages. Thus, we can obtain information on the *degree of ionization* of the plasma from the measured location of the line energies compared to what would be expected from the electron temperature (see Section 3.3.3). As well, at ionization parameters larger than $n_e t \sim 10^{12}\ s\ cm^{-3}$, no significant line energy shift from that of CIE is found for a wide range of electron temperatures and atomic numbers (Masai 1994). Figure 3.3 shows simulated X-ray spectra of NEI plasma models with different ionization timescales as would be detected with the *Chandra* observatory. For example, at low ionization timescales ($n_e t \sim 10^{10}\ cm^{-3}\ s$) the Fe-L emission at ~1.1 keV dominates over the Fe-K emission at ~6.4 keV. The opposite is observed at high ionization timescales ($n_e t \sim 10^{12}\ s\ cm^{-3}$), where no change from ionization equilibrium is seen.

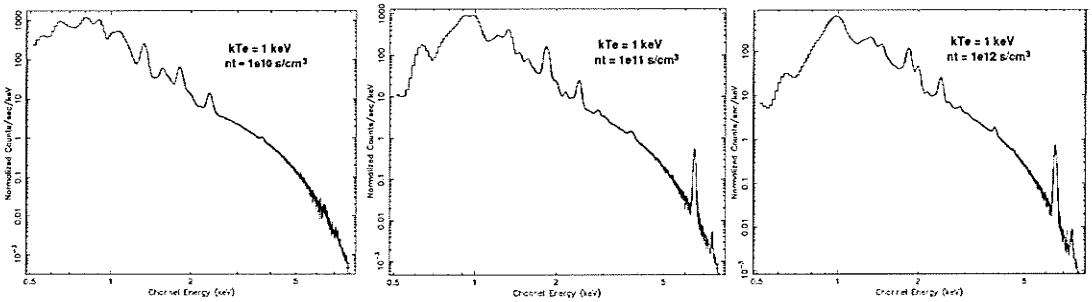

Figure 3.3: X-ray spectra with different ionization timescales convolved with the Chandra ACIS response (see Chapter 4). The electron temperature is 1 keV in all panels and ionization timescales are $1x10^{10}$, $1x10^{11}$ and $1x10^{12}$ cm^{-3} s, left to right. Abundances of all elements were fixed to their solar values (Anders and Grevesse 1989) and the column density of interstellar absorption, N_H, is $5x10^{21}$ cm^{-2}.

Furthermore, as shown by Hamilton, Sarazin and Chevalier (1983), the shape of the X-ray spectra for SNRs in the Sedov stage (see Section 1.2.2) is determined by just two parameters instead of three. They show that the shock temperature T_s and the collisional parameter $\eta \equiv n_0^2 E$ can be used to describe the state of the plasma. The latter parameter is independent of time and can be regarded as characterizing the rate at which the plasma relaxes toward equilibrium, equivalent to $n_e t$ above. Physical SNR parameters that can be derived using T_s, η, and the basic Sedov expansion law given by equation (1.3) are:

$$\upsilon_s = 839\left(\frac{T_s}{10^7 K}\right)^{1/2} km\, s^{-1} \tag{3.9}$$

$$n_0 t = 4015\left(\frac{\eta}{10^{51} ergs\, cm^{-6}}\right)^{1/3}\left(\frac{T_s}{10^7 K}\right)^{-5/6} yr\, cm^{-3} \tag{3.10}$$

$$t = 4015\left(\frac{\eta}{10^{51}\ ergs\, cm^{-6}}\right)^{-1/6}\left(\frac{T_s}{10^7 K}\right)^{-5/6}\left(\frac{E}{10^{51} ergs}\right)^{1/2} yr \tag{3.11}$$

$$r_s = 8.62\left(\frac{\eta}{10^{51}\ ergs\, cm^{-6}}\right)^{-1/6}\left(\frac{T_s}{10^7 K}\right)^{-1/3}\left(\frac{E}{10^{51} ergs}\right)^{1/2} pc \tag{3.12}$$

$$M_s = 96.8\left(\frac{T_s}{10^7 K}\right)^{-1}\left(\frac{E}{10^{51} ergs}\right) M_\odot \tag{3.13}$$

Here, υ_s is the shock velocity, n_0 is the pre-shock Hydrogen density, t is the age of the remnant, E is the supernova explosion energy, r_s is the shock radius, and M_s the swept-up mass of the ISM. A mean molecular weight of $\mu = 0.63 m_p$ and a total number to hydrogen density ratio of 2.34 were used to derive these equations.

Therefore, fitting a Sedov model to the thermal emission from the SNR gives values for T_s and $n_0 t (= n_e t / 4.8)$, which together with one extra parameter (such as r_s from image analysis) can give a complete set of Sedov parameters for the remnant. This model has been used in this thesis when estimating the parameters for G292.0+1.8 (see Section 5.5.2).

3.3.3 Thermal bremsstrahlung

Bremsstrahlung, or braking radiation, results from the acceleration of electrons in Coulomb collisions with other electrons or with ions and nuclei. The most common situation is the emission from a hot gas as the electrons collide with nuclei due to their random thermal motions. This is called 'thermal bremsstrahlung' or 'free-free' emission and represents one of the main processes responsible for continuum thermal emission from SNRs. Thermal bremsstrahlung, also called free-free emission, produces a characteristic spectrum. The distribution of photon energies produced by bremsstrahlung reflects the electron energy distribution, and has an average that is proportional to temperature. Thus, a measurement of the spectrum can be used to determine the temperature of the gas.

The shape of the thermal bremsstrahlung spectrum is given by a total continuum emission per unit frequency, volume, and time as follows

$$P_\nu^{ff} = \frac{dW(T,\omega)}{d\omega dV dt} = \frac{2^5 \pi e^6}{3mc^3}\left(\frac{2\pi}{3mk}\right)^{1/2} T^{-1/2} Z^2 n_e n_i e^{-h\nu/kT} \bar{g}_{ff}(T,\nu) \qquad (3.14)$$

where m is the electron mass, T the plasma temperature, n_e the electron density, n_i the ion density, Ze the ion charge and $\bar{g}_{ff}(T,\nu)$ is the velocity-averaged Gaunt factor. In cgs units, the above flux is then given by

$$P_\nu^{ff} = 6.8\times10^{-38} T^{-1/2} Z^2 n_e n_i e^{-h\nu/kT} \bar{g}_{ff}(T,\nu)\ erg\ s^{-1}\ cm^{-3}\ Hz^{-1} \qquad (3.15)$$

(Rybicki and Lightman 1979). Thus, the only dependence of the bremsstrahlung spectrum on frequency is through $e^{-h\nu/kT}$ and $\bar{g}_{ff}(T,\nu)$. For energies in the range $h\nu/kT \sim 10^{-4}$–1,

$e^{-h\nu/kT}$ ~1–2.7 and $\bar{g}_{ff}(T,\nu)$ ~1–5. For high energies, $h\nu/kT >> 1$, the exponential term dominates and cuts off the spectrum close to the limit ν_{cut}, which is related to the interaction time between the electron and the ion. Therefore, the bremsstrahlung spectrum is nearly a constant for a given gas temperature and it allows us to estimate the temperature of astrophysical objects. Figure 3.4 shows a modeled bremsstrahlung spectrum (left) and a simulated one as would be detected with *Chandra*. The specific shape of the simulated *Chandra* spectrum is affected by instrumental effects. As discussed in Section 3.2, interstellar absorption plays an important role at low energies.

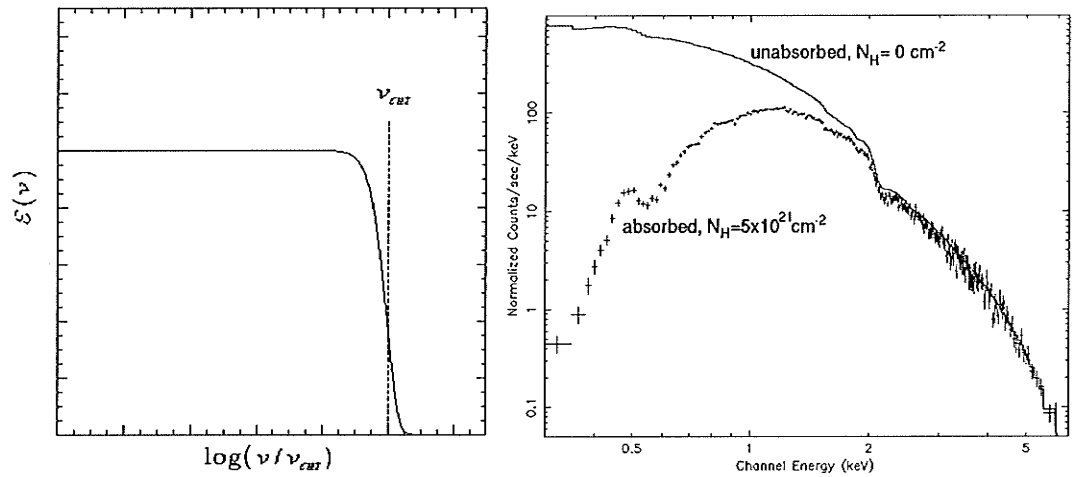

Figure 3.4: Flat spectrum produced in the bremsstrahlung process (left). Simulated bremsstrahlung X-ray spectrum for a gas at a temperature of 1 keV as measured with Chandra, both an unabsorbed (column density of 0 cm^{-2}) and absorbed (5x10^{21} cm^{-2}) spectra are shown (right).

3.4 Nonthermal emission

Nonthermal emission from SNRs arises from synchrotron radiation of highly energetic particles accelerated at the shock front of the supernova blast wave or a confined pulsar wind.

Synchrotron radiation

A relativistic electron moving at a velocity, υ, in the presence of a magnetic field of strength, B, moves in a helical path around the field line, and consequently emits synchrotron radiation. For plerions, the powering pulsar is thought to provide the relativistic electrons and magnetic field. For shell-type SNRs, the electrons and fields originate from the shocked ISM.

For a homogeneous and isotropic ensemble of electrons producing nonthermal synchrotron radiation, the energy density distribution, $n(\gamma)$, has a power law form

$$n(\gamma)d\gamma = n_0\gamma^{-\Gamma}d\gamma \tag{3.16}$$

The ensemble spectrum will then be given by

$$P_\nu = \frac{2}{3}c\sigma_T n_0 \frac{U_B}{\nu_L}\left(\frac{\nu}{\nu_L}\right)^{-(\Gamma-1)/2} \tag{3.17}$$

(Rybicki and Lightman 1979), where $\sigma_T = 8\pi e^4/3m^2c^4$ is the Thompson cross section, $U_B = B^2/8\pi$ is the energy density of the B-field and ν_L is the non-relativistic Larmor frequency.

Therefore, a power law electron energy distribution with photon index, Γ, will produce a power law spectrum with spectral index of $-(\Gamma-1)/2$. Figure 3.5 shows the single electron and integrated synchrotron spectrum (left) as well as a simulated one as detected with *Chandra* (right).

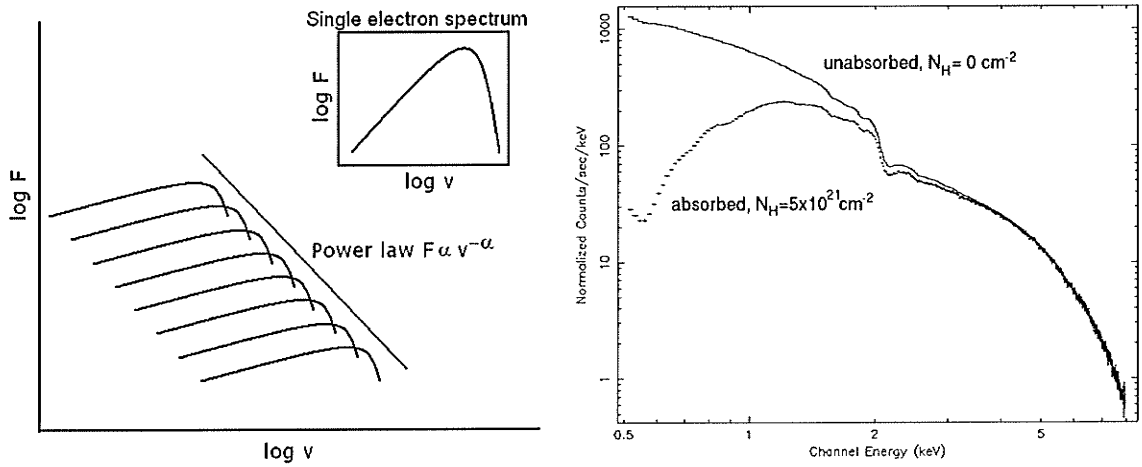

Figure 3.5: The power law spectrum of synchrotron radiation (left) and a synchrotron spectrum with photon index $\Gamma = 2$ as detected with Chandra (right).

3.5 Summary

Supernova remnants and pulsars offer a wide range of observational studies. Spatial studies of these objects allow for the determination of their morphology and subsequent classification, as well as the ability to resolve their different components: forward shock, ejecta-dominated regions, pulsar and PWN. Spectral studies are useful in the determination of the emission mechanism and subsequent properties of the emitting material, such as:

temperature, chemical composition, elemental abundances, ionization state, spectral index, etc. This thesis deals with the high-resolution, high-sensitivity X-ray studies of two composite Galactic supernova remnants, G292.0+1.8 and G292.2-0.5. The X-ray analysis of these objects allows us to study their plerionic emission, their underlying engines, and the properties of the ambient medium in which they are expanding and with which they are interacting.

Chapter 4

The Chandra X-ray Observatory

4.1 Historical Overview of X-ray Telescopes and their Instruments

The progress in our understanding of the properties of pulsars and SNRs at X-ray wavelengths has been shaped by the evolution of the telescopes used to observe them. The first X-rays of cosmic origin were detected in 1949, when radiation detectors aboard rockets were carried above the atmosphere and detected X-rays coming from the Sun. More than a decade later, improved detectors discovered X-rays coming from sources beyond the solar system when NASA launched the *Uhuru X-ray Satellite* in the early 1970's. Over the next three decades, advances in X-ray astronomy were possible with the launch of the *Einstein, ROSAT, ASCA and Chandra* observatories, among others. Table 4.1 summarizes the main properties of these telescopes. The technical information presented throughout this chapter was compiled from the *Chandra X-ray Center* (CXC, http://cxc.harvard.edu/)

	Spatial Resolution (arcsec)	**Energy Range (keV)**	**Area at 1 keV (cm^2)**	**FOV (arcmin)**	**Spectral Resolution $(E/\Delta E)$**	**Timing Resolution**
Chandra	HRC = 0.4 ACIS = 0.5	0.1–10.0	800	HRC = 30 ACIS = 16(I), 8x48(S)	ACIS = 20–50	HRC = 16 μs ACIS = 3.2 sec
ASCA	GIS = 30 SIS = 30	0.5–12.0	350	GIS = 50 SIS = 22	GIS = 1–15 SIS = 9–40	GIS = 63 ms SIS = 2, 4, 8 sec
ROSAT	HRI = 2 PSPC = 30	0.1–2.4	400	HRI = 38 PSPC = 60	PSPC = 1–4	HRI = 61 μs PSPC = 0.1 ms
Einstein	IPC = 60 HRC = 5	0.2–20.0	200	IPC = 75 HRC = 25	HRC = 0.5–1 FPCS = 100–1000	IPC = 63 ms HRC = 8 ms

Table 4.1: Characteristics of different X-ray satellites. Credit: HEASARC (http://heasarc.gsfc.nasa.gov /docs/corp/observatories.html). See 'Abbreviations' section at the end of the manuscript for acronyms.

NASA's *Einstein* Observatory, launched in 1978, was the first large X-ray telescope with mirrors. The *Roentgensatellit* (*ROSAT*), a joint satellite project between Germany, the United Kingdom and the United States, carried an even larger X-ray telescope than *Einstein* into orbit in 1990. The *ASCA* satellite was launched in 1993 and was the first X-ray astronomy telescope that employed CCD cameras in addition to having a significant effective area above 2 keV. However, the capabilities offered by the use of CCDs aboard *ASCA* were not fully explored due to the uncertainties in the calibration and response of the mirrors. Therefore, the launch of NASA's *Chandra X-ray Observatory* and its CCD cameras marked the next leap in X-ray astronomy in making full use of the capabilities offered by these instruments.

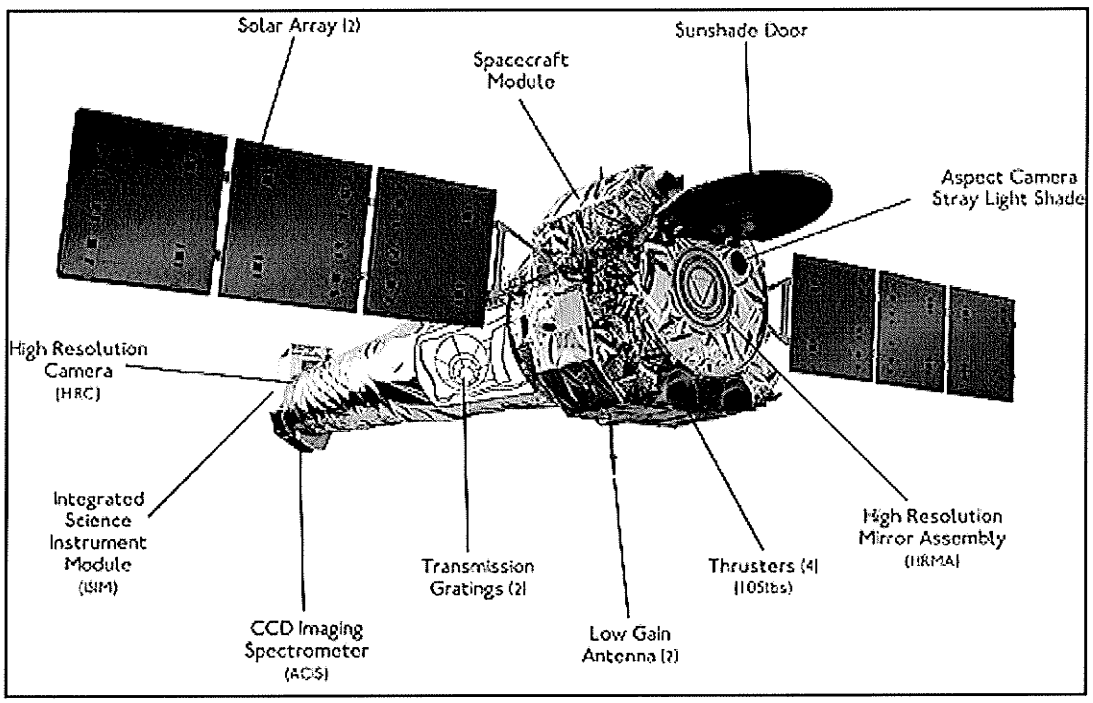

Figure 4.1: Major components of the Chandra X-ray Observatory. Credit: CXC/RTW. Available at http://chandra.harvard.edu/resources/illustrations/art_illus1.html.

4.2 The *Chandra X-ray Observatory*

4.2.1 Overview

The *Chandra X-ray* Observatory (CXO, formerly the Advanced X-ray Astrophysics Facility [AXAF]) was launched by the Space Shuttle Columbia on July 23, 1999. After an Inertial Upper Stage boosted the satellite out of a low-earth orbit and separated from the telescope, *Chandra* fired its own Integral Propulsion System several times to put the telescope in a highly elliptical orbit. The final orbit has a perigee of 1.0×10^4 km, an apogee of 1.4×10^5 km (approximately one-third the distance to the moon) and an orbital period of 64 hr. The telescope uses a grazing incident optic (the High Resolution Mirror Assembly, or HRMA) that allows spatial resolution of better than 0.5″. Figure 4.1 is a schematic of the main components that make up the *Chandra* observatory. The capabilities offered by these mirrors are fully used by the CCD detectors coupled with them. The Advanced CCD Imaging Spectrometer (ACIS) and the High Resolution Camera (HRC) are the two primary focal plane instruments employed by *Chandra*. The ACIS detectors have excellent spatial resolution (one pixel = 0.5″), moderate spectral resolution ($E/\Delta E \sim 20-50$ [1]) and high detection efficiency (~20–90%) in the 0.2–10 keV band. The HRC is a microchannel plate with similar characteristics to the HRI cameras in *Einstein* and *ROSAT*. Both the HRC and ACIS have two separate arrays, an imaging array (HRC-I and ACIS-I) intended for wide field imaging and a spectroscopic array (HRC-S and ACIS-S) to be used in conjunction with

---

[1] Shortly after launch, some of the ACIS detectors suffered radiation damage, degrading their resolution compared to pre-flight performance. See Section 4.2.2.

transmission gratings that can be inserted into the optical path. Figure 4.2–Figure 4.4 compare *Chandra*'s spatial resolution, spectral resolution and detection efficiency to that of *Einstein, ROSAT and ASCA.* The superior image resolution offered by *Chandra* and the excellent overall performance of the ACIS detector can be seen in these plots. In the following, a description of the major satellite components is provided, stressing the capabilities offered by ACIS since data from this detector was used for this thesis. A detailed description of all the components can be found at the CXC website[2].

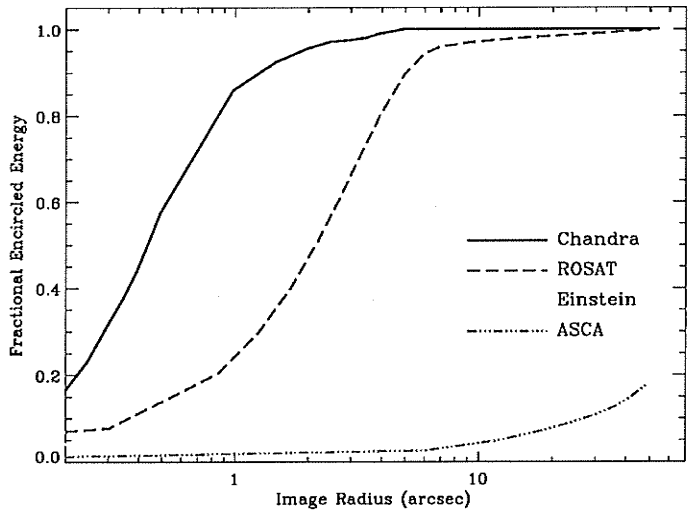

Figure 4.2: Comparison of Chandra's spatial resolution with that of Einstein, ROSAT and ASCA. Einstein, ROSAT and ASCA performances measured at 1.49 keV, the Chandra performance is between 0.5–2.0 keV. Adapted from Pivovaroff (2000).

[2] http://cxc.harvard.edu/

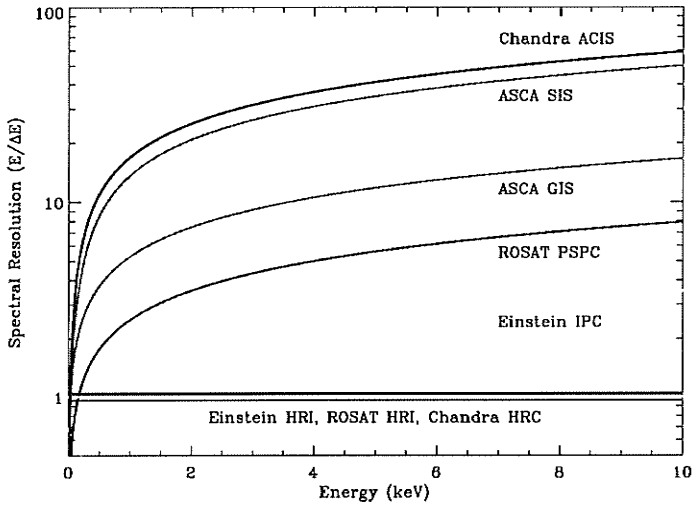

Figure 4.3: Same as above but showing energy resolution ($E / \Delta E$) as a function of energy. Adapted from Pivovaroff (2000).

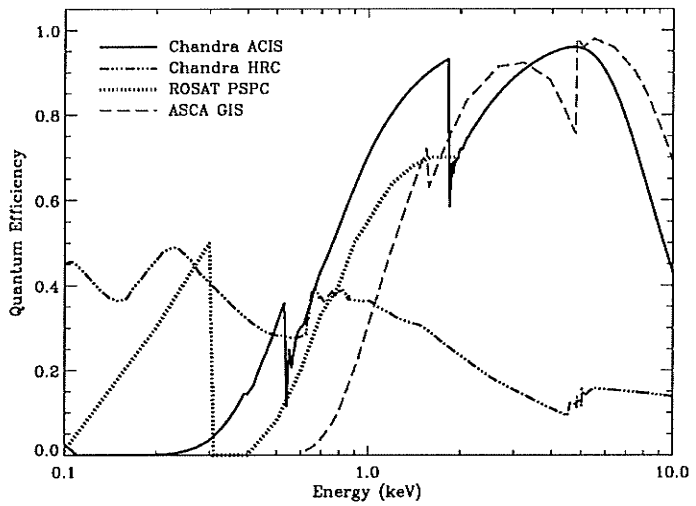

Figure 4.4: Same as above but showing quantum efficiency (QE) as a function of energy illustrating the detection efficiency of the detectors. Adapted from Pivovaroff (2000).

4.2.2 Advanced CCD Imaging Spectrometer

ACIS offers the capability to provide high-resolution images and moderate resolution spectra. It consists of ten individual CCDs, each of 1024x1024 pixels, arranged in two separate arrays. The engineering model and schematic view of ACIS at the focal plane are shown in Figure 4.5. Four of the chips were placed in a 2x2 array (ACIS-I) with a 17'x17' FOV intended for imaging of extended objects. The other six chips were arranged in a 1x6 array (ACIS-S) intended primarily as a read-out detector for the High Energy Transmission Grating (HETG). However, two of the CCDs in ACIS-S are back-illuminated (see below) and offer superior low-energy detection efficiency than the rest of the chips. Imaging observations with moderate spectral resolution using ACIS-S are then common.

The ACIS CCDs, built at MIT, have been optimized for high detection efficiency (0.2–0.9), superior energy resolution ($E/\Delta E$ ~20–50) and good spatial resolution (0.5" when combined with the HRMA) in the 0.2–12 keV band. In general, CCDs are a series of Metal Oxide Semiconductors (MOS) capacitors packed together for operation as a single array composed primarily of Silicon. The charge generated through photo-absorptions is collected in a potential well and is then transferred (clocked) from neighboring capacitors to an amplifier stage, where the resultant output is converted from an analog to a digital signal by read-out electronics (see the CXC website for further details).

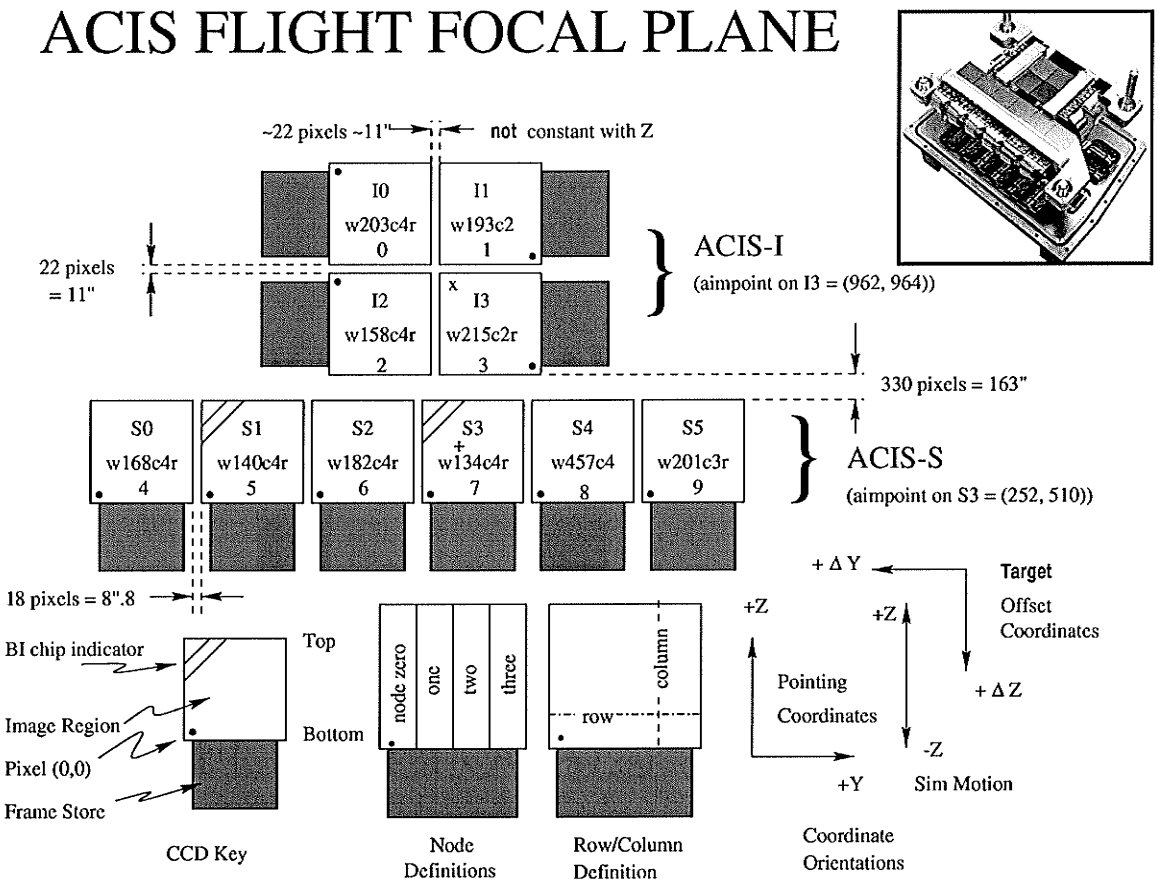

Figure 4.5: Engineering model (inset) and schematic drawing of ACIS, showing both the imaging and spectroscopy arrays. Credit: NASA/CXC/SAO. Available at http://cxc.harvard.edu/proposer/POG/html/ACIS.html.

Normally, radiation is incident to the surface of the CCD that has "gates". A "gate" structure on one surface of the CCD defines the pixel boundaries by alternating voltages on three electrodes spanning a pixel. Thus, photons must first pass through the gate structure before they can interact in the depleted silicon (the region below the gates where most of the absorption takes place). These devices are then called front-illuminated (FI). At low

energy (E < 2 keV), the characteristic absorption length of photons is comparable to the thickness of these structures, reducing the low-energy detection efficiency. One approach for increasing the low energy detection efficiency is to reverse the orientation of the device, such that the radiation does not have to propagate through the gates to interact in the depleted silicon. A device operated in this fashion is referred to as back illuminated (BI). In turn, BI chips have lower high energy (E > 5 keV) efficiency, increased non-linearity and diminished spectral resolution than FI CCDs. Therefore, the choice of device depends on its application and the specific scientific objectives of the observation. Two of the chips in the ACIS-S array are BI (see Figure 4.5). Originally, the FI chips on ACIS had spectral resolution closer to the theoretical limit than did the BI chips. However, shortly after launch, their spectral resolution was degraded due to low energy protons encountered during radiation belt passages and reflecting off the X-ray telescope onto the focal plane. The BI CCDs were not impacted since it is far more difficult for low energy protons from the direction of the HRMA to deposit their energy in the buried channels of the BI devices. Thus, the energy resolution for the two BI devices in ACIS-S remains close to pre-launch values. In particular, the performance of the BI ACIS-S3 chip (see Figure 4.5) is well calibrated, behaves as expected and was then used for the observations analyzed in this thesis.

Photoelectric absorption of an X-ray in Silicon results in the liberation of a proportional number of electrons to the incident photon energy (an average of one electron-hole pair for each 3.7 eV of photon energy absorbed). Immediately after the photoelectric interaction, the charge is confined by electric fields to a small volume near the interaction site. However, charge in an FI device can also be liberated below the depletion region (in an inactive

substrate) from where it diffuses into the depletion region. This charge may easily appear in two or more pixels. The CCD's spectral resolution depends on an accurate determination of the total charge deposited by a single photon. This in turn depends on the fraction of charge collected, the fraction of charge lost in transfer from pixel to pixel during read-out, and the ability of the readout amplifiers to measure the charge. Spectral resolution also depends on read noise and the off-chip analogue processing electronics.

4.3 *Chandra* Data Processing

The above advantages offered by the *Chandra* observatory can only be fully implemented if the data obtained from it is carefully processed. It is possible to analyze any *Chandra* data straight from the pipeline (see below). However, to get scientifically accurate results, there are a number of data processing questions that should be considered separately for individual observations.

The calibration files that are required for standard processing and analysis of *Chandra* data are stored and indexed in the *calibration database* directory (also called "CALDB"). The data reduction and subsequent analysis of *Chandra* data performed for this thesis were performed with the *Chandra Interactive Analysis of Observations* (CIAO) v2.2 system. A detailed description of the following issues and the analysis recipes followed during this thesis can be found at http://cxc.harvard.edu/ciao/threads/all.html.

4.3.1 Standard Data Processing

The Chandra X-ray Center (CXC, operated by the Marshall Spaceflight Center) performs standard data processing (or "pipeline") on all Chandra science data. The processing runs in several stages or "levels", each of which is built on the results of the preceding level. A well-defined set of data products are made at the end of each level. The processing levels relevant to this thesis are as follows:

1. Level 0 (L0): processing carried out by the CXC which takes raw *Chandra* spacecraft telemetry and splits it into convenient FITS files. The telemetry is then divided along the observation boundaries. These products are not used for user-level analysis.
2. Level 1 (L1): takes L0 output and applies instrument-dependent corrections, such as the change in the pointing position of the telescope with time. This processing is also carried out by the CXC. The L1 outputs have not had anything irreversible done to the data (e.g. no photon event rejection). These products represent the starting point for the processing carried out in this thesis.
3. Level 2 (L2): takes L1 outputs and applies standard, but irreversible, corrections that cause information to be lost and cannot be regained from the L2 products alone. This processing includes filtering the events file on the good time intervals (GTIs, see Section 4.3.6), cosmic ray rejection, etc. A "finished" event file is produced, which is then used to perform the necessary imaging and spectral analysis.

4.3.2 Charge Transfer Inefficiency

The loss of charge in a CCD as it is shifted from one pixel to the next during readout is known as charge transfer inefficiency (CTI). When X-rays (and cosmic rays) deposit charge in an ACIS CCD, the charge is read out using one of four sets of read-out electronics. Each read out is used for a specific 256x1024 pixel subset (node) of the CCD. Since charge is read out at only one location on a node, the charge at all other locations must be moved to the read out. Charge is moved both vertically (i.e. in the "parallel" direction) and horizontally (i.e. in the "serial" direction). The total number of pixels through which charge must be moved depends on the location at which charge is deposited on the CCD. As charge is moved, some may be lost to charge traps that are distributed across the detector and cause CTI to occur.

CTI affects the measured spectral distribution of astrophysical sources in two ways:

1. Since some of the charge is trapped, the amount of charge read out is less than the amount of charge deposited. This effect causes the measured pulse-height distribution (see below) for a source to be shifted to lower pulse heights (i.e. lower measured energies than originally present in an event).
2. For a variety of reasons, CTI causes degradation in the energy resolution of a CCD. The measured pulse-height distribution of a mono-energetic source (or a line feature) is then broadened.

These effects are functions of the location in a CCD where an X-ray interacts since they depend on the number of traps through which charge is moved. The algorithm CTICORRECTIT was developed by Townsley et al. (2000) to estimate the amount of

charge originally deposited on one of *Chandra*'s CCDs in one event. This correction makes use of the amount of charge read out and the location of the recorded event on the detector. This CTI correction was the first reduction technique applied to the level 1 *Chandra* data used in this thesis. A new level 1 file is produced from which a final event 2 file is obtained by applying all of the remaining corrections summarized below.

4.3.3 ACIS Gain Map

The total charge per pixel detected for an individual event is called the event's pulse height amplitude (PHA). For a given CCD location, a gain table is used to map the PHA of an event to its corresponding physical energy value. In turn, the energy value is converted into a pulse invariant (PI) value through the equation $PI = [(energy / 14.6\ keV) + 1]$, where PI is in units of detector energy channels. PI spectral data can then be added (binned) according to the specific needs of a particular scientific analysis. Therefore, using the correct gain map is especially important if one is interested in performing spectral analysis on ACIS data. In this thesis, the latest available gain file (CALDB v2.12) was applied to the level 1 data using the CIAO tool ACIS_PROCESS_EVENTS with the option *gradefile=CALDB*.

4.3.4 Pixel Randomization

The level 1 data obtained from the pipeline randomizes the positions of events detected within a given ACIS pixel. This randomization is done to remove the instrumental "gridded" appearance of the data and to avoid possible aliasing effects associated with this spatial

grid. The event coordinates are randomized over the instrument pixel size (0.5 arcsec), so no information is lost. However, disabling pixel randomization can improve the resolution of on-axis Chandra sources and was thus performed on the data used for this thesis. This correction was applied by setting the parameter *rand_pix_size=0.0* while running the ACIS_PROCESS_EVENTS tool on the event 1 file.

4.3.5 Event Grades

An event is registered by a CCD when the charge generated by photoelectric absorption is drawn into the electrostatic potential well created by the gates. If the charge is confined to one pixel, a single pixel event results. If an interaction takes place close to a pixel boundary, the charge will be collected by two neighboring pixels (a split event), and if an interaction takes place near a pixel corner the charge can be divided between three or four pixels (also a split event). During processing, an island of pixels is considered in which the center pixel is the local maximum and is also above an event threshold value, T_e. If surrounding pixels are above a split threshold value, T_s (where $T_s < T_e$), their signal is added to the central pixel's and the event is classified according to the distribution of charge in the island of pixels. On the basis of this pattern, the event is assigned a "grade". Depending on the grade, the data are then included in the telemetry.

Table 4.2 represents the mapping between grades and event types used for *Chandra* data analysis. The proportion of events in each event grade is a strong function of photon energy. As the initial charge cloud size and the mean interaction depth increase with photon energy,

the probability of a split event increases. The larger the interaction depth, the larger the contribution of diffusion to the charge cloud size, and therefore, the larger the probability that the event will occupy more than one pixel. During processing of the data used in this thesis, only grades 0, 2, 3, 4, and 6 were selected using the tool DMCOPY with the option *grade=0,2,3,4,6*.

Table 4.2: Grades and their corresponding X-ray event types

Grade	Event Type
0	Single pixel
1	Diagonal split
2	Vertical split
3,4	Horizontal split
5	L-shaped split with corners
6	L-shaped and Square
7	All pixel split

In addition, event grades contain information about the origin of an event. As high-energy particles (e.g. electrons and protons) pass through a CCD, they deposit a significant amount of ionizing radiation, generating in some cases as many as several hundred events. However, these events usually have charge deposited in at least five or six pixels of the islands of pixels discussed above. As the grades of these types of events (grades 1, 5 or 7)

are not part of the standard processing, particle-induced background events can be effectively discriminated purely on the basis of event grade.

4.3.6 Good Time Intervals

A list of good time intervals (GTI) is supplied by the pipeline, containing observation periods that are not excluded due to bad conditions, such as high background or unstable pointing position. A level 2 file will have been properly screened by selecting only those observing times contained in the GTI list. This selection was performed using the tool DMCOPY and the option *@gti_file_name*.

4.3.7 ACIS background

The ACIS background consists of a relatively soft Cosmic X-ray Background (CXB) contribution and cosmic ray-induced events with a hard spectrum. Most cosmic ray events can be filtered out by applying a grade filter (e.g., rejecting the above ASCA grades 1, 5 and 7). After such filtering, the CXB component and the cosmic ray component are comparable below ~2 keV (during the quiescent background intervals, see below) and the cosmic ray component dominates above that energy, consistent with the pre-launch estimates.

A phenomenon that can seriously affect the scientific value of an observation is background flares, when the count rate can increase by a factor of up to 100. Such flares have been observed everywhere in *Chandra's* orbit. They are most prominent in the BI chips

but also affect the FI chips. The nature of these flares is under investigation. The flares are easily seen when making light curves of a source-free region in the CCD chip with the tool DMEXTRACT and it is usually best to discard the time intervals with flares present.

During the quiescent periods and after the standard event screening (see Section 4.3.5), the ACIS background appears to be relatively constant with time. This weak dependence of the quiescent background on time allows us to use other observations (cleaned for flares using exactly the same criteria) for modeling the background. A number of source-free observations have been combined to create experimental quiescent background event files. These "blank-sky" datasets can then be adapted to individual observations and the resulting files used to estimate the background during both imaging and spectral analysis.

In addition, if source-free sky regions are available in the same observation and in adjacent spatial regions to the sources being studied, the spectrum from these regions can be used to estimate the background during spectral analysis.

4.3.8 ACIS background in VFAINT mode

There are a number of telemetry formats available in which the ACIS CCDs can be operated. Specifying a format determines the type of information that is included in the telemetry stream. The number of bits per event determines the event rate at which the telemetry will saturate and data will be lost until the on-board buffer empties. For this thesis, data obtained in telemetry formats "Faint" and "Very Faint" were used. The "Faint" format provides the event position in detector coordinates, an arrival time, an event amplitude, and

the contents of the 3x3 pixel island that characterizes the event grade.

The "Very Faint" format provides the event position in detector coordinates, the event amplitude, an arrival time, and the pixel values in a 5x5 pixel island. This offers the advantage of reducing the ACIS particle background by screening out events with significant flux in border pixels of the 5x5 event islands. The 5x5 event islands recorded in the Very Faint mode reveals that a large number of events are in fact the end-points of big particle tracks. A standard grade analysis using 3x3 islands, fails to screen these events. Several examples are shown in Figure 4.6. Such events can then be screened by rejecting those in which any border pixel in the 5x5 island is above the split threshold T_s. This correction was applied by using the ACIS_PROCESS_EVENTS tool and setting the option *check_vf_pha=yes*.

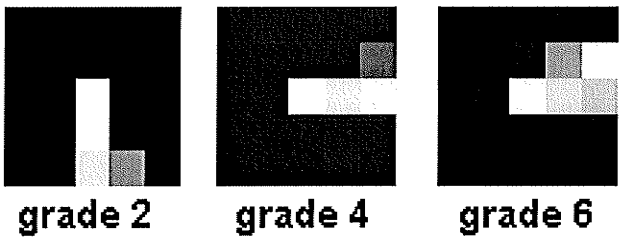

Figure 4.6: Example grades assigned to events detected in a 5x5 pixel island.

4.4 *Chandra* Imaging Analysis

An example of the image obtained from the original level 2 data for the SNR G292.0+1.8 is shown in Figure 4.7 (left). By extracting a spectrum of the whole remnant (Figure 4.7, right),

the presence of emission lines at low energies becomes apparent. The level 2 data can then be divided into different energy ranges according to the observed spectrum using the DMCOPY tool with the option *energy=min_energy:max_energy*, where *min_energy* and *max_energy* are the chosen low and high energy ranges, respectively. For example, the data can be divided into the 0.3–1.15 keV, 1.15–2.15 keV and 2.15–10.0 keV X-ray bands in order to isolate the spatial regions which most contribute to the emission at these energies. The derived images are shown in Figure 4.8.

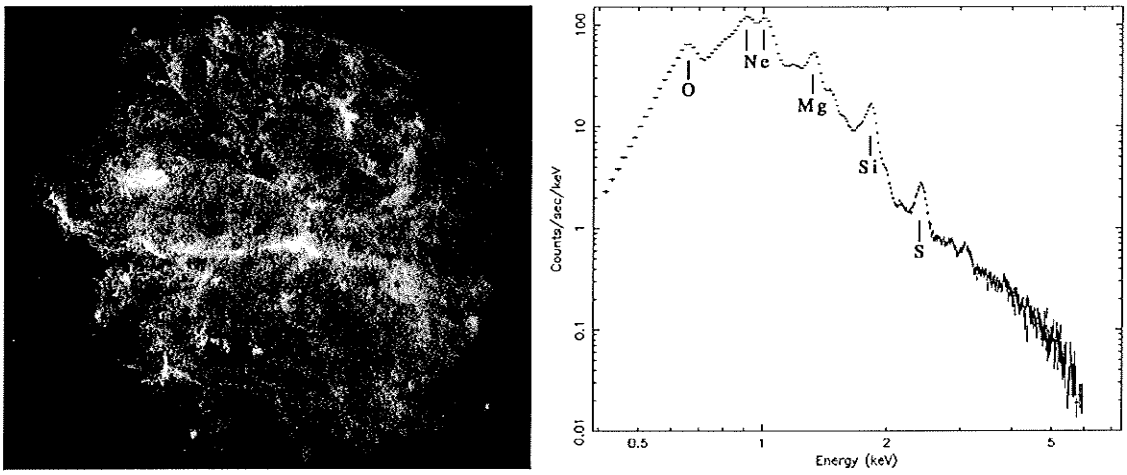

Figure 4.7: Left – 0.3–10.0 keV raw image of the remnant G292.0+1.8 obtained with Chandra. Right – Overall spectrum of the remnant.

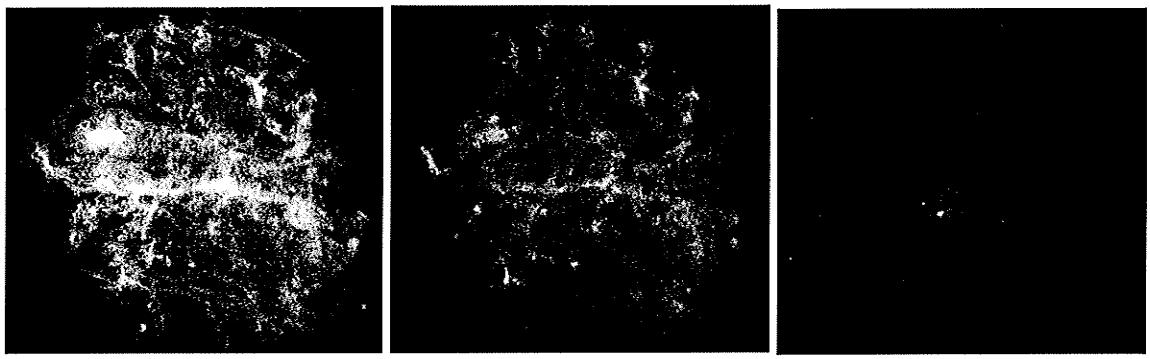

Figure 4.8: Raw Chandra images of the remnant G292.0+1.8 in the 0.3–1.15 keV (left), 1.15–2.15 keV (center) and 2.15–10.0 keV (right) bands.

In addition, any image can be further processed by applying a "Gaussian smoothing" algorithm to it. The purpose of this step is to 'blur' the image in such a way as to remove noise, however at the expense of removing detail as well. A 2-D symmetric Gaussian distribution has the form $\frac{1}{2\pi\sigma}\exp\left(-\frac{x^2+y^2}{2\sigma^2}\right)$, where σ is the standard deviation of the distribution. The degree of smoothing (called 'smoothing scale' or 'kernel size') to be performed is determined by the size of σ. The smoothing is then carried out by producing a discrete approximation of this function (=kernel) and 'sliding' it over the image continuously in order to multiply them until the whole original image is covered. This processing was performed on the images shown in this thesis with the tool CSMOOTH, which also allows for the possibility of using different kernel sizes (if desired) according to each pixel's significance above the background. For example, the same images shown in Figure 4.8 were smoothed using this tool and a σ=1.5", the resulting images are shown in Figure 4.9.

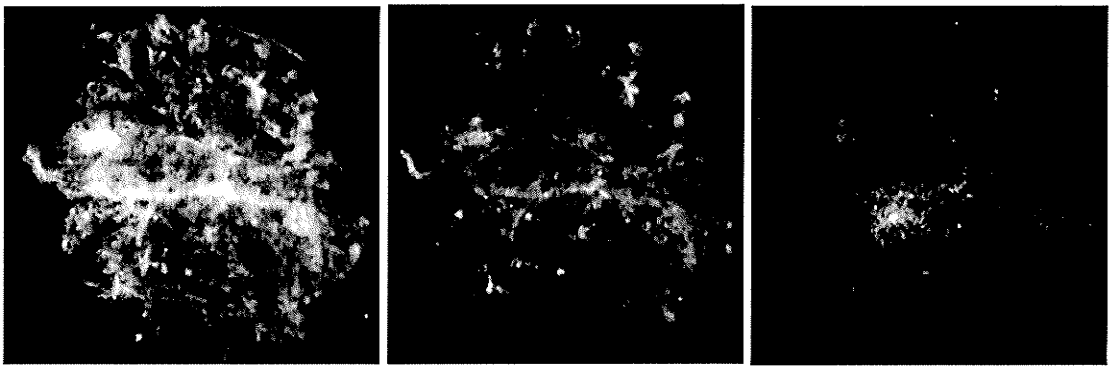

Figure 4.9: Same images as in Figure 4.8 but each smoothed with a Gaussian with σ =1.5".

The above images can then be color-coded using programs such as 'Photoshop'[3] or 'Gimp'[4] and then combined to create 'true-color'[5] images of the objects being studied. In this way, the images shown can be given red (0.3–1.15 keV), green (1.15–2.15 keV) and blue (2.15–10.0 keV) colors and subsequently superimposed to produce a final image (see Figure 4.10)

---

[3] http://www.adobe.com/products/photoshop/main.html

[4] http://www.gimp.org/

[5] In this context at X-ray energies, a 'true-color' image refers to false-color images in which the color refers to energy, i.e. combined energy-coded images

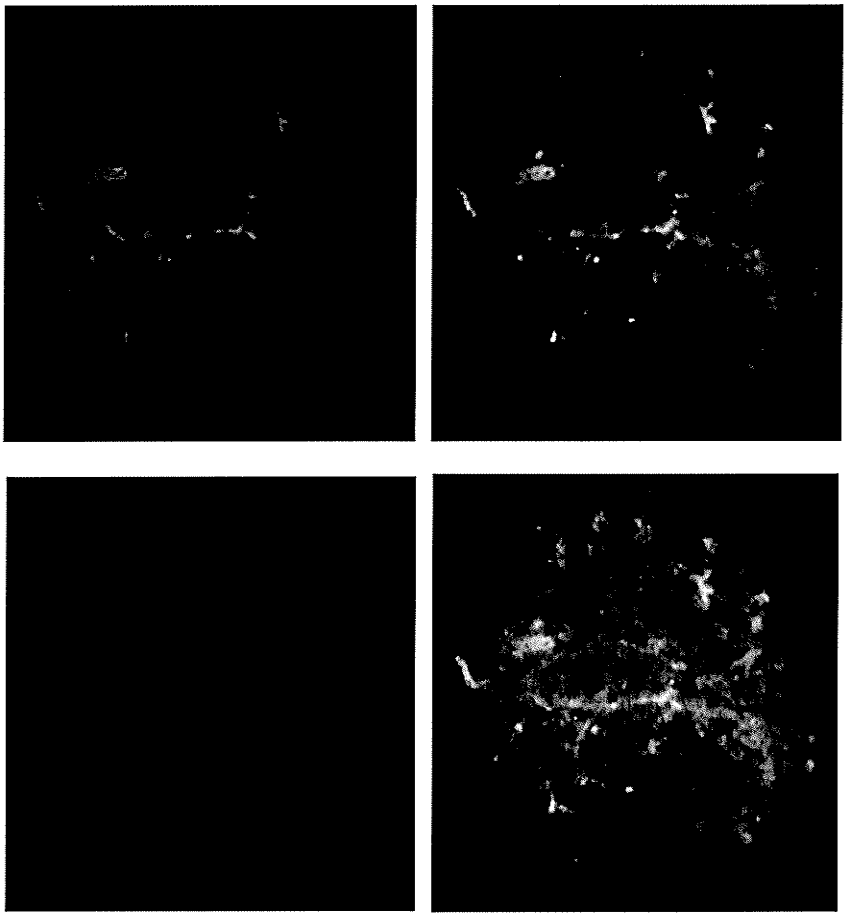

Figure 4.10: Color-coded, smoothed images in the 0.3–1.15 keV (top left, red), 1.15–2.15 keV (top right, green) and 2.15–10.0 keV (bottom left, blue) bands. The brightness and contrast for each image were adjusted and they were then combined to create a 'true-color' image (bottom right).

4.5 Summary

The imaging and spectral capabilities offered by *Chandra* represent an order of magnitude improvement over previous X-ray astronomy missions. For the purposes of this thesis, the excellent spatial resolution and moderate spectral resolution offered by the ACIS detector

(and in particular the un-degraded performance of the back-illuminated ACIS-S3 chip) offers the best combination to study the X-ray emission from the SNRs G292.0+1.8 and G292.2–0.5 and their associated pulsars. The unprecedented spatial resolution offered by *Chandra* allows for the study of their individual components, from separating the different emission regions in SNRs to resolving small PWN structures surrounding the pulsars. The available spectral resolution also makes it possible to study the different emission mechanisms present in these systems. And finally, the high detection efficiency allows for the possibility to detect fainter objects.

Chapter 5

The SNR/PSR system G292.0+1.8 and J1124–5916

5.1 Introduction

Chandra has been advancing our understanding of core-collapse supernovae by revealing their collapsed cores and their outflows, the distribution of supernova ejecta, and their interaction with the interstellar medium (ISM). Increasing the sample of SNRs with hybrid morphology (i.e. composite-type SNRs) helps address questions related to the birth properties and evolution of neutron stars and SNRs in the ISM.

G292.0+1.8 (MSH 11-54) offers a unique laboratory to address these questions because of its hybrid morphology, its youth, and its size. This SNR is one of three Oxygen-rich remnants in our Galaxy. It was first discovered in the radio band (Milne 1969; Shaver & Goss 1970), where it exhibits a centrally-filled morphology, indicative of the presence of a PWN. *Einstein* and *EXOSAT* X-ray observations classified the remnant as a type-II explosion of a massive star (Hughes & Singh 1994). The low resolution *Einstein* image of the remnant is shown in Figure 5.1. Recent *Chandra* observations led to the discovery of the long-sought PWN (Hughes et al. 2001; Safi-Harb & Gonzalez 2002) surrounding a candidate pulsar. An imaging study of the SNR with *Chandra* (Safi-Harb & Gonzalez 2002; Park et al. 2002) traced the distribution of the ejecta. The remnant has a morphology similar to Cas A on small scales (Hwang, Holt, & Petre 2001), however, no Fe-K line-emission was detected.

The discovery of the PWN in G292.0+1.8 prompted a deep search for radio pulsations and led to the discovery of a 135 ms pulsar, J1124–5916, coincident with the *Chandra* X-ray point source (Camilo et al. 2002a). J1124–5916 has a derived spin-down luminosity $\dot{E}$ of 1.2×10^{37} erg s^{-1}, a surface magnetic dipole field strength of 1×10^{13} G, and a characteristic age of 2,900 yrs. The pulsar's spin parameters are summarized in Table 5.1. To date, the only estimate of the age of this SNR is from optical studies of the high-velocity material coincident with the PWN (Murdin & Clark 1979). The optical spectrum is dominated by Oxygen and Neon emission lines with a velocity of ~2,000 km s^{-1}, giving the remnant an age of 1,600 years, a factor of 1.8 less than the characteristic age of the pulsar.

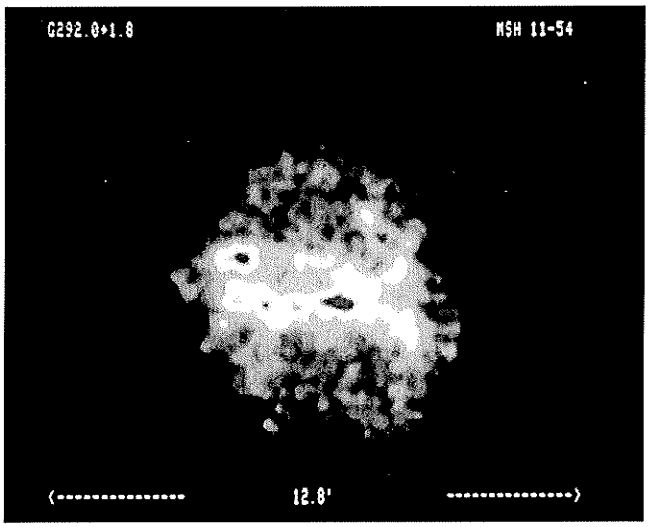

Figure 5.1: Low resolution Einstein image of the remnant G292.0+1.8. Credit: K. P. Singh. Available at http://tifrc1.tifr.res.in/~singh/SNR1.html.

For this thesis, the first detailed spatially resolved spectroscopy of the *Chandra* observation was performed in order to infer the energetics of the supernova explosion, the

mass of the progenitor, the age of the remnant, and the parameters of the pulsar wind.

Parameter	Value
R.A. (J2000.0)[a]	11 24 39.1
Decl. (J2000.0)[a]	−59 16 20
Period, P (s)	0.1353140749(2)
Period derivative, $\dot{P}$	$7.471(2) \times 10^{-13}$
Epoch (MJD)	52,180.0
Dispersion measure, DM (cm^{-3} pc)	330(2)
Data span (MJD)	52,157–52,214
Number of TOAs	10
rms timing residual (ms)	5.8
rms timing residual, "whitened" (ms)	0.4
Flux density at 1400 MHz, S_{1400} (mJy)	0.08(2)
Derived parameters:	
Characteristic age, τ_c (yr)	2900
Spin-down luminosity, $\dot{E}$ (ergs s^{-1})	1.2×10^{37}
Magnetic field strength, B (G)	1.0×10^{13}
Distance, d (kpc)[b]	~5
Radio luminosity, L_{1400} (mJy kpc^2)	~2

NOTE.—Numbers in parentheses represent 1 σ uncertainties in the least significant digits quoted.

[a] Position known with ~1″ accuracy from *Chandra* data (Hughes et al. 2001). Units of right ascension are hours, minutes, and seconds, and units of declination are degrees, arcminutes, and arcseconds.

[b] Distance of SNR G292.0+1.8

Table 5.1: Parameters derived for PSR J1124–5916. From Camilo et al. (2002a).

5.2 Observations and Data Reduction

G292.0+1.8 was observed with the S3 chip of the Advanced CCD Imaging Spectrometer (ACIS) on board *Chandra* on March 11, 2000. The CCD temperature was -120°C with a frame readout time of 3.2 sec in "faint" telemetry mode. A correction for Charge Transfer Inefficiency (CTI) was done by applying the CTICORRECTIT tool to the event 1 raw data (Townsley et al. 2000). A new event 2 file was then obtained by screening the data to the standard status, *ASCA* grades, and flight timeline filter configurations, using standard Ciao

v2.2 routines. The 0.5″ pixel randomization was also removed. The lightcurve from source-free regions in the S3 chip was inspected and no significant background flares were found. The resulting exposure time was 38 ksec (~10.5 hrs).

5.3 Imaging analysis

Figure 5.2 shows the 'true-color' broadband image of G292.0+1.8. This image was obtained by combining individual images in the soft (0.3–1.15 keV, red), medium (1.15–2.15 keV, green) and hard (2.15–10.0 keV, blue) X-ray bands, each smoothed with a Gaussian with σ=1.5″. The soft and medium images show a filamentary structure ranging from arcsecond to arcminute scales. The hard band image (blue) shows an unresolved point source surrounded by a hard nebula, as found by Hughes et al. (2001).

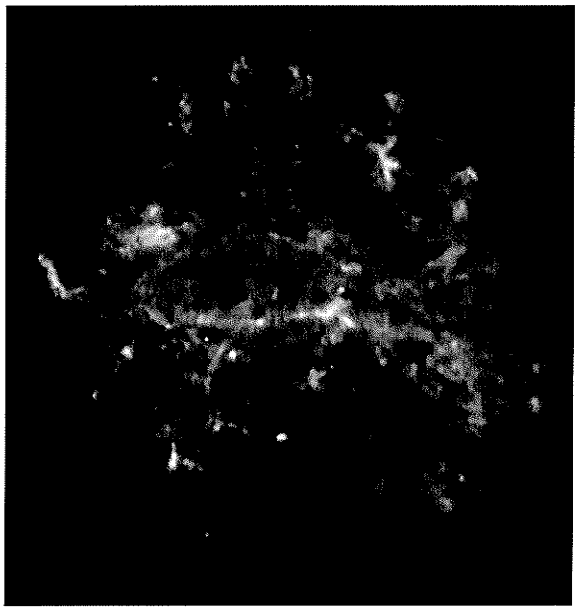

Figure 5.2: 0.3–10.0 keV X-ray image of the remnant. Images in the soft (0.3–1.15 keV, red), medium (1.15–2.15 keV, green) and hard (2.15–10.0 keV, blue) bands were combined, each smoothed with a Gaussian with σ =1.5". The hard band contribution has been enhanced. The image size is 8'x8'.

The overall spectrum of the remnant (Figure 5.3, left) reveals that the thermal emission is dominated by O, Ne, Mg, Si and S lines (no Fe-K is present). Images of the remnant for each of these elements were created by selecting only the energy ranges in which each line dominates the spectrum. Their combined image is shown in Figure 5.3 (right). To estimate the background for these line images, the *Marx* software available through the *Chandra X-ray Center* was used to simulate a broadband continuum image. For the spectral input, a two-component bremsstrahlung model (to account for the cool and hot components that compose the continuum spectrum) was used. For the spatial distribution, a line-free image in the 4.0–6.0 keV was used as a template. (As a consistency check, continuum images were

extracted from line-free regions bracketing the centroids of the line images and were found to produce a morphology similar to that obtained with the simulated *Marx* images). Each simulated background image was then subtracted from the original line+continuum image, and smoothed with a Gaussian with σ=1.5″.

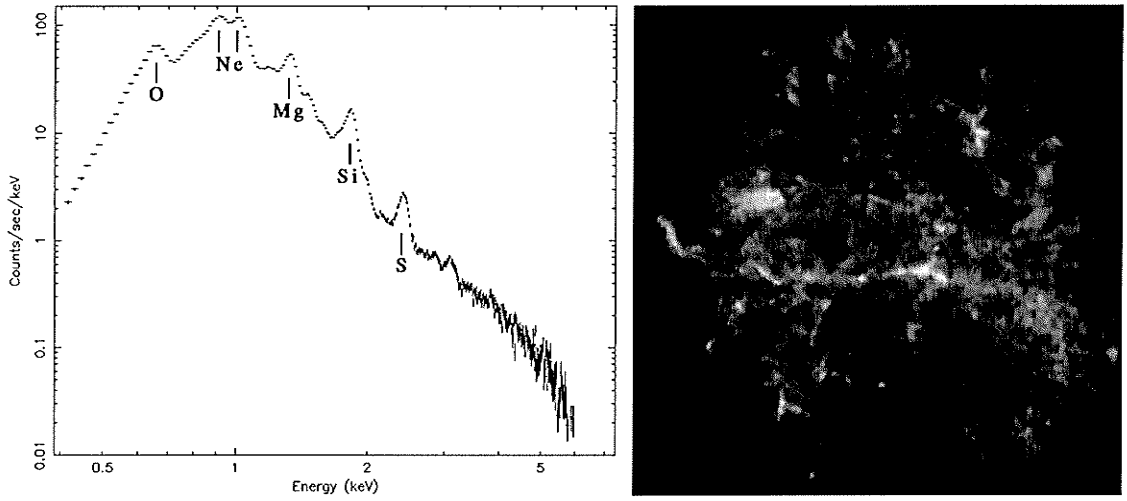

Figure 5.3: Left – Overall Chandra spectrum of G292.0+1.8 with dominant lines labeled. Right – Combined background subtracted line images; elements used were Oxygen (0.60–0.72 keV, red), Neon (0.74–1.10 keV, green), Magnesium (1.25–1.42 keV, cyan), Silicon (1.67–2.09 keV, blue) and Sulfur (2.26–2.59 keV, purple). The Si and S contribution have been enhanced.

5.4 Sub-arcminute spatially resolved spectroscopy

5.4.1 SNR G292.0+1.8

The excellent spatial resolution offered by *Chandra* allowed for the study of the spectral properties of the SNR on sub-arcminute scale. To perform spatially resolved spectroscopy of

the SNR, the 23 bright regions shown in Figure 5.4 were selected for analysis. Each spectrum obtained from the individual regions was fitted in the 0.5–8.0 keV range using the nonequilibrium ionization (NEI) model, VPSHOCK (Borkowski, Lyerly, & Reynolds 2001) in version 11.0.1 of the XSPEC package (Arnaud 1996). This model is appropriate for modeling plane-parallel shocks in young SNRs whose plasma has not reached ionization equilibrium. It is characterized by the shock temperature, kT, and the ionization timescale, $n_e t$, of the plasma. Here, n_e is the post-shock electron density and t is the time since the passage of the shock. In this case, t can then be used as a lower estimate on the SNR age. Since the remnant is ejecta-dominated, the abundances were allowed to vary. Appendix A summarizes the best fit parameters to all 23 regions obtained from these fits.

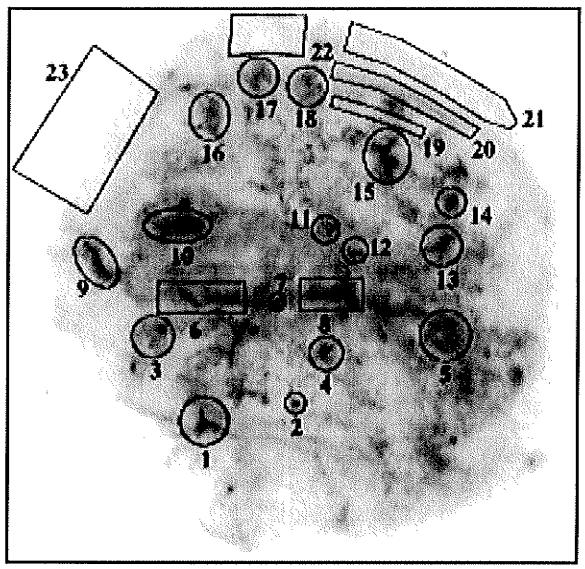

Figure 5.4: Regions selected to perform spatially resolved spectroscopy on the remnant G292.0+1.8.

One-component NEI model fits yielded an average temperature for the selected regions of

0.9±0.3 keV, with minimum and maximum values of 0.6 and 1.7 keV, respectively (see Appendix A). The ionization timescale varied across the SNR from ~5×10^{10} to ~10^{13} cm^{-3} s. These values indicate that the emission from the ejecta contains a wide range of temperatures and ionization states. Regions 1, 3, 7, 8 and 9 (see Figure 5.4) in the southeast of the remnant exhibit high ionization timescale values, indicating that the plasma has reached ionization equilibrium in the southeast. Relative abundances were well constrained in these models and were used to derive the abundance ratios discussed in Section 5.5.2.

Fitting the remnant with two-component models was then attempted. This was motivated by the expectation of a high-temperature and a low-temperature plasma associated with the supernova blast wave and reverse shock, respectively (see e.g. Safi-Harb et al. 2000). While the overall fits were slightly improved, the abundances could not be well constrained due to the large number of free parameters. The derived average temperatures for the hot and cool components were 1.05±0.34 keV and 0.37±0.18 keV, respectively (see Appendix A). These are lower than $1.64^{+0.3}_{-0.2}$ keV, as reported by Hughes & Singh (1994) from their one-component NEI model fit to the *Einstein* and *EXOSAT* data. The discrepancy is probably due to the contamination by the previously unresolved PWN.

5.4.2 Pulsar Wind Nebula

Chandra observations of PWNe have shown that:

1) PWNe harbor torus- and jet-like structures indicating equatorial and polar outflows, and

2) The power law photon index steepens away from the pulsar, as expected from synchrotron and expansion losses (see e.g. Safi-Harb 2002 for a review).

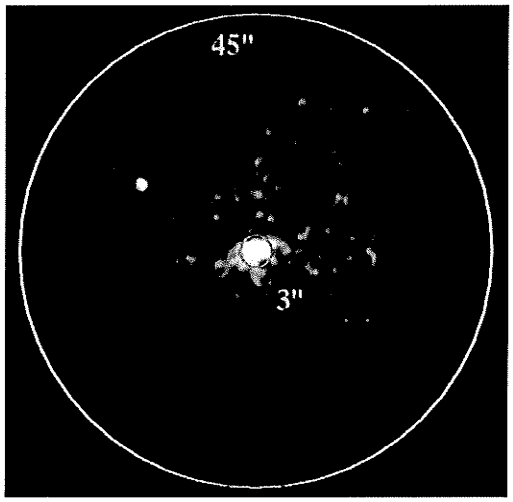

Figure 5.5: 2.6–10.0 keV image of the PWN surrounding PSR J1124–5916. The image was smoothed using a Gaussian with σ =0.25". The inner circle is at a radius 3" (R_s), and the outer one at 45" (R_n). See Section 5.5.3 for details.

By examining the PWN surrounding PSR J1124–5916 detected with *Chandra*, there is evidence of an arcsecond-scale east-west elongation and an extension to the south (see Figure 5.5), hinting at structures associated with the deposition of the pulsar's wind energy into its surroundings. To search for spectral variations, the inner 45" of the PWN was divided into four concentric rings to obtain enough counts to extract a spectrum. As reported by Hughes et al. (2001), the spectrum of the PWN is heavily contaminated by thermal emission from the SNR. In order to minimize this contamination, a nearby region was used as

background and the fit was restricted to the 1.5–7.0 keV range, thus reducing the contamination from Oxygen, Neon, and Magnesium ejecta.

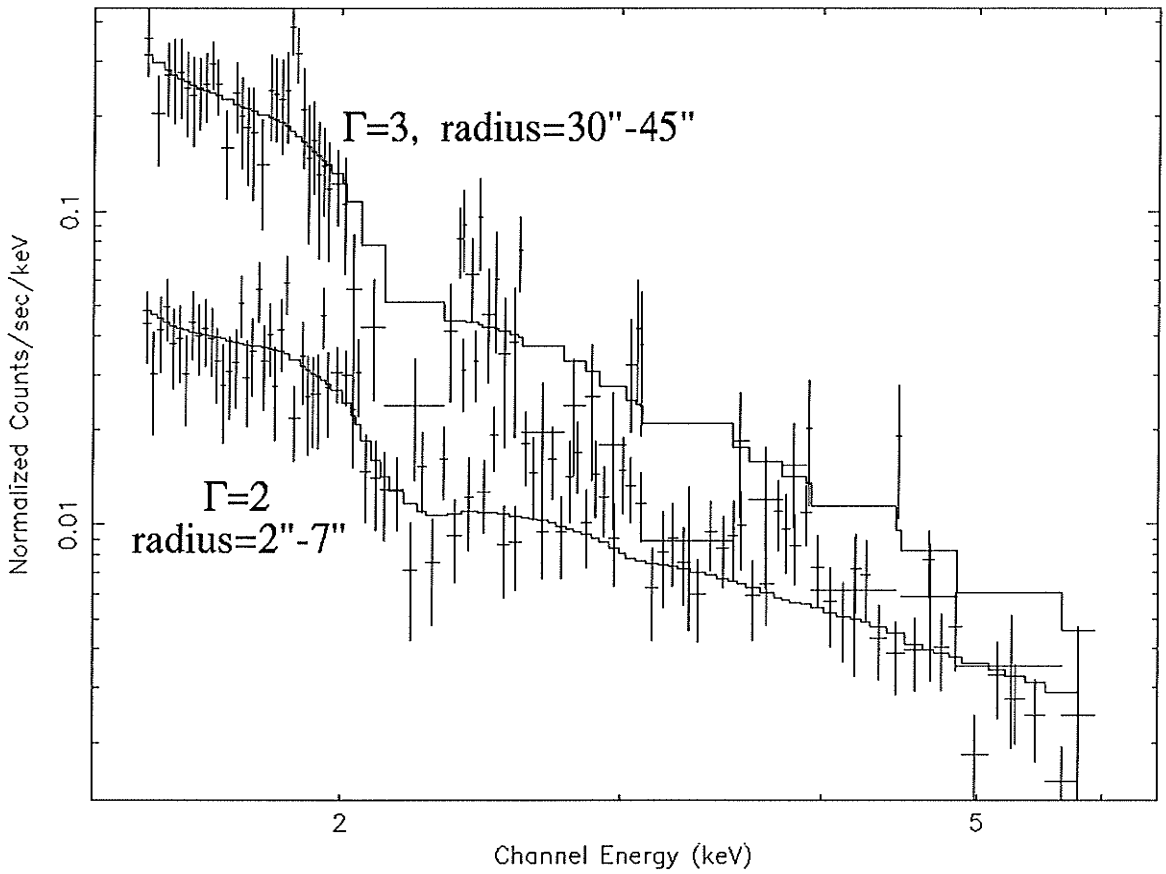

Figure 5.6: Sample 1.5–7.0 keV spectra of the PWN surrounding J1124–5916. The steepening of the power law index can be seen from the inner (2"–7") radii to the outer (30"–45") radii. See Table 5.2 for best fit parameters.

Using a power-law model, we find a steepening of the photon index, Γ, from 1.9±0.1 to 3.0±0.2 between the inner and outer ring when N_H was fixed to our best fit value for the

pulsar of $(3.7 \pm 0.4) \times 10^{21}$ cm^{-2} (see Table 5.2 and Figure 5.6). This result is expected from synchrotron losses and is reminiscent of Crab-like nebulae (e.g. Safi-Harb et al. 2001). Fitting the inner 45" at once, we find an average photon index Γ=2.6±0.1 and unabsorbed X-ray flux of $f_X = 7.4 \times 10^{-11}$ erg cm^{-2} s^{-1} in the 0.5–10 keV band.

Radius	Γ (± 90%)	χ^2(dof)
<2" (pulsar)	1.74±0.10	142 (140)
2"–7"	2.0±0.10	122 (94)
7"–15"	2.06±0.11	129 (125)
15"–30"	2.37±0.10	202 (219)
30"–45"	3.00±0.20	204 (212)

Table 5.2: Steepening of the power law photon index, Γ, of the PWN in G292.0+1.8. The value for N_H was fixed during fitting to the best value for the pulsar of 3.7×10^{21} cm^{-2}.

5.5 Discussion

5.5.1 Distance

Combining the best fit parameters from the one- and two-component fits to all 23 regions (see Appendix A), the average SNR column density is $N_H = (5 \pm 1) \times 10^{21}$ cm^{-2}. We can use this value to verify previous estimates for the distance to G292.0+1.8 using the strong correlation found between the visual extinction produced by dust (A_V) and X-ray absorption produced by both dust and cold gas (N_H) (Predehl & Schmitt 1995). The extinction per unit

distance in the direction of the remnant can be estimated from the contour diagrams given by Lucke (1978): $E_{B-V}/D \sim 0.2$ mag kpc^{-1}. Using the relation $N_H/A_V = 1.79\times10^{21}$ cm^{-2} mag^{-1}, which translates into $N_H/E_{B-V} = 5.55\times10^{21}$ cm^{-2} mag^{-1} (Predehl & Schmitt 1995), we derive a distance of 3.6–5.5 kpc. A distance of 4.8 kpc, as used in previous studies, is then a good approximation and will be adopted in the following discussion.

5.5.2 Supernova Parameters

The results from our NEI model fits to the emission from the SNR can be used to derive the supernova parameters. In the standard picture of the X-ray emission from young SNRs, the cool component arises from shocked ejecta, and the hot component is usually attributed to the blast wave shocking the surrounding medium. The spatially resolved spectroscopy described in Section 5.4.1 indicates that most of the regions in the SNR (except for the PWN and regions 21–23) are well fitted with a one-component NEI (VPSHOCK) model with high metal abundances (with respect to solar), indicating that these knots are the shocked ejecta associated with the explosion of a massive star.

Nucleosynthesis yield as a function of the progenitor's mass has been numerically computed by Woosley and Weaver (1995) among others. Relative abundances were well constrained in the one-component NEI model fits to the ejecta-dominated regions (#1–20) and were used to derive the abundance ratios, $R_{X/Si}$, of element X to Silicon. These ratios are sensitive to the mass of the progenitor star in nucleosynthesis models, and can be used to infer the progenitor's mass. Figure 5.7 shows the average values for these ratios along

with their rms scatter. Over-plotted are the predicted ratios from nucleosynthesis models for progenitors of 25, 30, 35 and 40 $M_{\odot}$. The measured ratios are then consistent with a progenitor's mass of 30–40 $M_{\odot}$.

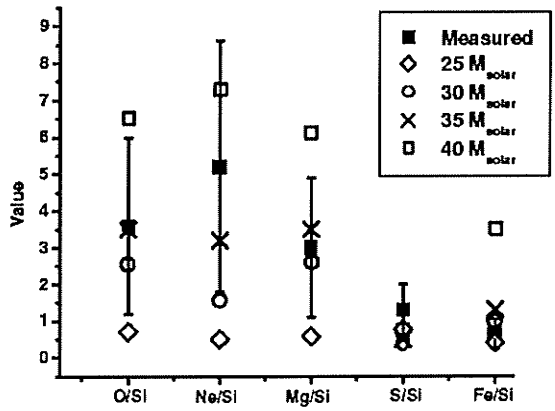

Figure 5.7: Average abundance ratios (filled squares) and their rms scatter measured throughout the remnant. Predicted ratios from nucleosynthesis models are also shown.

Regions 20–23 selected in the analysis are of special interest (see Figure 5.4). Region 20 is part of a set of sharp circumferential filaments surrounding the bulk of the ejecta-dominated X-ray emission. Regions 21, 22 and 23 are part of an outer faint ridge of emission delimiting the SNR. For comparison, the one- and two-component NEI fits to regions 20 and 21 are summarized in Table 5.3. It is likely that regions 21–23 indicate the location of the blast wave shocking the surrounding medium for the following reasons: 1) as shown in Table 5.3, the abundances derived for region 21 using one-component models are consistent with ISM abundances (sub-solar) and are the lowest ones throughout the remnant, while those derived for region 20 are contaminated by ejecta; 2) the outermost emission is absent in the equivalent width maps which reveal the ejecta (Park et al.

2002); and 3) even two-component model fits to regions 21–23 require sub-solar abundances, which is not the case for region 20, where both components require above-solar abundances. Thus, if regions 21–23 represent the current location of the supernova blast wave, the derived NEI values for these regions can then be used to estimate some basic physical parameters as discussed in Section 3.3.2.

	Region 20	Region 21
	One-component Fits	
N_H (10^{21}cm^{-2})	4.7 ± 0.2	4.9 ± 0.3
kT (keV)	$0.66^{+0.01}_{-0.03}$	0.87 ± 0.07
$n_e t$ (cm^{-3} s)	$(7.5^{+2.4}_{-1.8}) \times 10^{11}$	$(8.7 \pm 2.4) \times 10^{10}$
O abundance$_\odot$	1.1 ± 0.1	$0.38^{+0.04}_{-0.06}$
Ne abundance$_\odot$	0.90 ± 0.06	$0.53^{+0.05}_{-0.06}$
Mg abundance$_\odot$	$0.63^{+0.05}_{-0.06}$	0.23 ± 0.06
Si abundance$_\odot$	0.47 ± 0.06	$0.27^{+0.09}_{-0.08}$
S abundance$_\odot$	1.2 ± 0.3	$0.2^{+0.4}_{-0.2}$
Fe abundance$_\odot$	0.24 ± 0.02	0.16 ± 0.03
norm	$(3.3 \pm 0.2) \times 10^{-3}$	$(1.4 \pm 0.2) \times 10^{-3}$
χ^2_ν (dof)	1.9 (119)	1.2 (98)
	Two-component Fits	
N_H (10^{21} cm^{-2})	6.1 ± 0.03	$6.1^{+0.02}_{-0.01}$
kT_{hot} (keV)	$0.94^{+0.05}_{-0.02}$	$0.95^{+0.20}_{-0.15}$
$n_e t_{hot}$ (cm^{-3} s)	$(3 \pm 0.5) \times 10^{11}$	$(6^{+1.4}_{-1.8}) \times 10^{9}$
norm$_{hot}$	$(1.05 \pm 0.05) \times 10^{-3}$	$(9.1 \pm 1.4) \times 10^{-4}$
kT_{cool} (keV)	0.27 ± 0.02	0.84 ± 0.06
$n_e t_{cool}$ (cm^{-3} s)	$(2.7\ ^{+2.3}_{-1.1}) \times 10^{11}$	$(1.4 \pm 0.3) \times 10^{11}$
norm$_{cool}$	$(5.1 \pm 0.4) \times 10^{-3}$	$(2.8^{+0.3}_{-0.2}) \times 10^{-4}$
χ^2_ν (dof)	1.6 (116)	1.0 (95)

Table 5.3: One- and two-component VPSHOCK fits to regions 20 and 21 in the SNR G292.0+1.8. The normalization (norm) is given in units of $\left(10^{-14} / 4\pi D^2\right) \int n_e n_H dV\ cm^{-5}$, *where* D *is the distance to the source (in cm) and* n_e, n_i *are the electron and ion densities (in cm^{-3}).*

First, the derived values for the ionization timescale, $n_0 t$, from regions 21–23 can be used as a lower limit for the age of the remnant, t, by using the observed emission measure (EM, or normalization) as an estimate for the ambient density, n_0. For this, the values from the more reliable one-component fits in the 0.5–8.0 keV band were used. The corresponding SNR size would be $r \sim 4.2'$=5.9 pc (at 4.8 kpc). In the following example, the parameters derived for region 21 (shown in Table 5.3) are used. The observed EM of 0.09±0.02 (after scaling it to the SNR volume) corresponds to $\int n_e n_H dV = 10^{14}\left(4\pi D^2\right)\left(EM\right)$ $= \left(2.5 \pm 0.6\right) \times 10^{58}$ cm^{-3}. If the emission volume $V = fV_{tot}$ (where f is the filling factor) and $n_e = 4.8 n_0 = 1.1 n_H$, we find an upstream density $n_0 = \left(0.23 \pm 0.03\right) f^{-1/2}$ cm^{-3}. Then, the best fit $n_0 t$ parameter from the VPSHOCK model (see Table 5.3) corresponds to a shock age of $t = 2,500^{+1100}_{-700} f^{1/2}$ years. Similarly, these parameters can be derived for regions 22 and 23 and are summarized in Table 5.4. For a reasonable filling factor of 0.25, the shock age varies from 1,250–4,450 years. The discrepancy between these ages suggests that the northeastern regions are shocked at earlier times than the western regions, probably due to an inhomogeneous medium. This complication makes the determination of the SNR parameters in this manner uncertain.

	Region 21	Region 22	Region 23
Ionization timescale, $n_e t$ (cm^{-3} s)	$(8.7\pm2.4)\times10^{10}$	$(2.1\pm0.6)\times10^{11}$	$(3.1^{+1.2}_{-0.6})\times10^{11}$
$\int n_e n_H \mathrm{dV}$ (10^{58} cm^{-3})	2.5 ± 0.6	3.9 ± 0.9	2.5 ± 0.8
Ambient density, n_0 ($f^{-1/2}$ cm^{-3})	0.23 ± 0.03	0.29 ± 0.4	0.23 ± 0.04
Swept-up mass, M_s ($f^{-1/2}$ $\mathrm{M}_\odot$)	6.7 ± 0.8	8.3 ± 0.9	6.7 ± 1.1
Lower age limit, t ($f^{1/2}$ years)	$2{,}500^{+1{,}100}_{-7{,}00}$	$4{,}900^{+2{,}100}_{-1{,}500}$	$8{,}900^{+5{,}700}_{-2{,}800}$

Table 5.4: Derived SNR parameters from NEI fits to forward shock regions 21, 22 and 23

Therefore, in order to estimate the global properties of the SNR independently of the small-scale density variations, an attempt was made to fit the spectrum of the whole remnant at once (see Figure 5.3, left). This proved to be extremely difficult using the entire 0.5–8.0 keV band and various combination models with up to three components. The difficulty is due to the large number of NEI components needed to account for the variations in temperature and ionization time-scale of the ejecta, as indicated in our spatially resolved spectroscopy described in Section 5.4.1. However, restricting the fit to the 2.0–8.0 keV range (to remove the contamination from O, Ne, Mg and Si ejecta) and excluding the pulsar and its PWN, a two-component model (VPSHOCK + SEDOV) provided an acceptable fit for the overall spectrum with $\chi^2_\nu(dof) = 1.17(197)$; SEDOV is an NEI model that accounts for the hot thermal emission from the SNR interior and is based on the Sedov dynamics (Borkowski et al. 2001). Although the remnant is not strictly in the Sedov phase but most probably in the transition state between the free expansion and Sedov phases (Hughes & Singh 1994, see Section 1.2), the Sedov approximation can be used to derive physical estimates for the SNR. In this way, the VPSHOCK model was used to characterize the

emission from the Sulfur ejecta, while the SEDOV model was used to characterize the blast wave component (abundances were set to 2/3 solar with equal electron and ion temperatures). Figure 5.8 shows the spectrum with best fit two-component model.

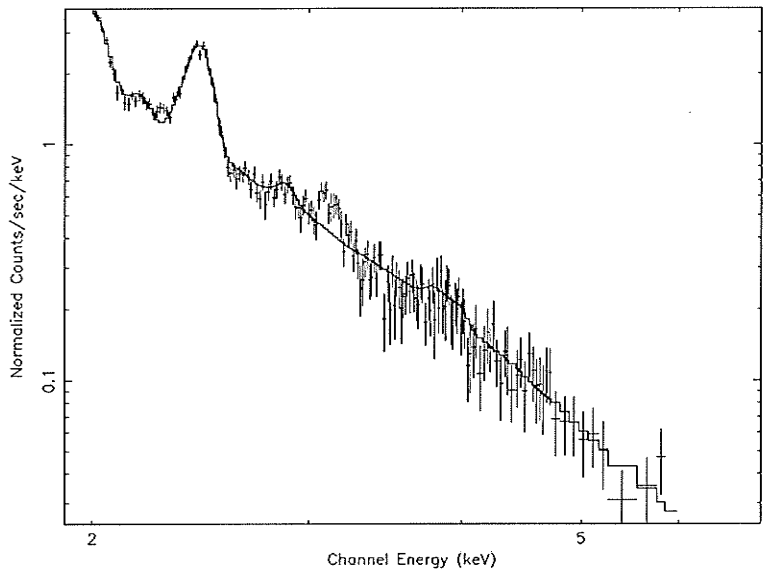

Figure 5.8: High-energy spectrum of G292.0+1.8 fitted with a two-component (VPSHOCK + SEDOV) model. See Table 5.5 for derived explosion parameters.

Table 5.5 then summarizes the derived parameters from the SEDOV model (EM, kT_s and $n_e t$) and the SNR parameters estimated from these values using the Sedov equations (3.9)–(3.13). First, the derived value for n_0 is consistent within the various uncertainties with that derived from the observed emission measure (see Table 5.4). The SNR age, t(Sedov)=2,400–2,850 yrs, is comparable to the average value also derived from regions 21–23 above. This age represents a more reliable estimate for the age of the

remnant since the contamination from ejecta has been minimized and the effect of an inhomogeneous medium has been averaged. In addition, this age is in close agreement with the pulsar's characteristic age of 2,900 years. This agreement strengthens the pulsar/SNR association and relaxes the need for invoking a very slow initial spin period or a non-canonical value for the braking index of the pulsar (Camilo et al. 2002a).

Parameter	Value ($\pm$ 1σ)
Emission Measure, EM	$0.166^{+0.006}_{-0.008}$
Shock temperature, kT_s (keV)	0.95 ± 0.15
Ionization timescale, $n_e t$ (cm^{-3} s)	$(2.0^{+0.4}_{-0.3}) \times 10^{11}$
Shock velocity, v_s (km s^{-1})	880 ± 70
Age, t (yrs)	$2{,}600^{+250}_{-200}$
Ambient density, n_0 (cm^{-3})	$0.51^{+0.15}_{-0.11}$
Explosion energy, E_0 (10^{51} ergs)	$0.18^{+0.08}_{-0.06}$
Swept-up mass, M_s ($M_\odot$)	$15.6^{+4.5}_{-3.5}$

Table 5.5: Explosion parameters derived from a Sedov fit to the hot component of the overall spectrum of SNR G292.0+1.8.

Recently, observations carried out with the Australia Telescope Compact Array (Gaensler & Wallace 2003) were able to resolve the positions of the forward and reverse shocks in the remnant at radio wavelengths. Using the model developed by Truelove and McKee (1999) for the evolution of a SNR and its shock structure, Gaensler & Wallace derive an expansion velocity of $1{,}200 d_6 / t_{2500}$ km s^{-1}, ambient density of $\sim 0.9 d_6^{-5/3} t_{2500}^{5/3}$ cm^{-3}, explosion energy of $\sim 1.1 \times 10^{51} d_6^{10/3} t_{2500}^{-1/3}$ ergs and ejected mass of $\sim 5.9 d_6^{4/3} t_{2500}^{5/3}$ $M_\odot$. Here, d_6 is the distance to the remnant in units of 6 kpc and t_{2500} is the age in units of 2,500 yrs (derived from the age

in Table 5.5 in conjunction with other estimates). Their estimates for the distance, ambient density and expansion velocity are broadly consistent with the ones derived in this work, while their estimate for the explosion energy is an order of magnitude higher.

5.5.3 Pulsar Wind Nebula Parameters

As noted by Hughes et al. (2001), the pulsar and its PWN are not located at the geometrical center of the remnant. The offset was attributed to either a high transverse velocity for the pulsar or slower expansion of the SNR toward the south-east. From the offset (~1′) they calculate a transverse velocity for the pulsar of $\sim 770\left(d_{4.8}/t_{1600}\right)$ km s^{-1}, where $d_{4.8}$ is the distance in units of 4.8 kpc and t_{1600} is the age of the remnant in units of 1,600 yrs. Using the new estimate of $2,600^{+250}_{-200}$ yrs for the age, this translates into a transverse velocity for the pulsar of $\left(470 \pm 40\right) d_{4.8}$ km s^{-1}. This value is in excellent agreement with recent estimates of the mean birth velocity of pulsars (450±90 km s^{-1}, Lyne & Lorimer 1994).

As mentioned above, the nearly east–west extension and jet-like structure extending to the south (see Figure 5.5) could be indicative of toroidal and collimated outflows reminiscent of Crab-like PWNe. The Kennel & Coroniti (1984a) model developed for the Crab can then be used to estimate some basic PWN parameters. In this model, the synchrotron nebula is produced by the confinement of a relativistic wind injected by the pulsar into its surroundings. The radius of the standing shock, R_s, is estimated by equating the pressure of the pulsar's wind, $\dot{E}/\left(4\pi c R_s^2\right)$, with the pressure in the nebula, $B_n^2/4\pi$ (see Section 2.3).

B_n, the nebular magnetic field, can be approximated from its equipartition value, $B_{n,eq}$. Equipartition assumes that the electron energy density is equal to the magnetic energy density (Katz 1987). This assumption is made since sources in which equipartition holds are, roughly, more efficient radiators and more likely to be observed than those in which it does not hold. In addition, the derived field through equipartition represents a lower limit estimate since the energy between the two reservoirs is minimized. The value for the field is then given by

$$B_{eq} \approx 2.3\left(10^{12}\,\frac{2\alpha+2}{2\alpha+1}\,\frac{\nu_2^{\alpha+1/2}-\nu_1^{\alpha+1/2}}{\nu_2^{\alpha+1}-\nu_1^{\alpha+1}}\,\frac{L}{V}\,k\right)^{2/7} G$$

(Lang 1999), where α, L and V are the nebula's spectral index, luminosity (in ergs s^{-1}) and volume (in cm^3), respectively. In turn, ν_1 and ν_2 are the lower and upper frequencies (in Hz) over which the luminosity is measured and k is typically taken to be 100 (Lang 1999).

Thus, using the average luminosity and spectral index for the PWN, the estimated nebular field from equipartition is $B_n \sim 1\times10^{-4}$ G. With the measured $\dot{E} = 1.2\times10^{37}$ ergs s^{-1} (Camilo et al. 2002a), this translates into a shock radius of $R_s \sim 3''$ at 4.8 kpc. Alternatively, the shock radius can be estimated using the thermal pressure in the SNR interior as a confining pressure. This average pressure can be estimated as $2n_e kT \sim 6.9\times10^{-9}$ erg cm^{-3}; which yields a shock radius of 1″. The inner circle shown in Figure 5.5 shows the estimated upper value of R_s.

An interesting parameter than can also be derived from *Chandra* studies of PWNe is the

pulsar wind magnetization parameter, σ, defined as the ratio of the Poynting flux to the particles flux, which can be estimated as $\sigma \sim (R_s / R_n)^2$, assuming a low value for σ (i.e. a particle-dominated wind, see Section 2.3). Using a shock radius R_s ~1″–3″ and a nebular radius R_n ~30″–45″, σ is estimated to be ~0.0005–0.01.

The properties of the PWN can thus be derived from the Kennel & Coroniti model. The value derived for the pulsar wind magnetization parameter in this manner is comparable to that derived for other PWNe of similar properties (Safi-Harb 2002). It is worth noting that the properties of the pulsar and the PWN in G292.0+1.8 are strikingly similar to those of the pulsar discovered in the Crab's cousin, G54.1+0.2 (Camilo et al. 2002b, Lu et al. 2002). The lack of ejecta and a shell in the latter SNR (and in a handful other plerions of comparable age) indicates that the classification of plerionic-type SNRs is to a large extent linked to the nature of the progenitor star, the explosion energy, and the environment.

Chapter 6

The SNR/PSR system G292.2–0.5 and J1119–6127

6.1 Introduction

For over three decades the Crab has been viewed as the standard model for young pulsars: a fast rotating neutron star with surface dipole magnetic field strength of 10^{12} G, injecting a relativistic magnetized wind of particles into its surroundings. The interaction of this wind with the surrounding medium creates the observable PWN. PWNe provide a unique laboratory that probes the properties of their powering engines, the physics of relativistic pulsar winds and their interaction with the interstellar medium (see e.g. Safi-Harb 2002 for a review). Recent observations have shown that a good fraction of young pulsars exhibit properties unlike the Crab. In spite of their youth, they have much larger spin periods and dipole magnetic fields (see e.g. Camilo et al. 2000). The search for their X-ray counterparts and any PWNe associated with them sheds light on their high-energy properties and the way these pulsars deposit their energies into their surroundings.

The radio pulsar J1119–6127 was discovered in the Parkes multi-beam pulsar survey (Camilo et al. 2000). It has a rotation period of 407ms, characteristic age of 1600 yrs, surface magnetic field strength of $4.1\times10^{13}\,G$, and spin-down luminosity $\dot{E}$ of $2.3\times10^{36}\ ergs\ s^{-1}$. This is an interesting and unusual object: although it is extremely young, it displays a relatively large period and magnetic field when compared to Crab-like pulsars. Its period derivative, $\dot{P}$, of 4×10^{-12} is one of the largest among radio pulsars. PSR J1119–

6127 is also one of a handful of pulsars for which a second period derivative $\ddot{P}$ has been measured, allowing for a calculation of the pulsar's braking index, giving $n = 2.91 \pm 0.05$ (see equation 2.8). This value makes J1119–6127 the pulsar with a braking index closest to the expected value of $n = 3$ if the pulsar slows down due to magnetic braking.

Following the pulsar's discovery, radio observations were performed with the Australia Telescope Compact Array (ATCA). They revealed a ring-like shell of 15′ in diameter surrounding the pulsar with a nonthermal spectrum characteristic of a shell-type SNR (Crawford et al. 2001). It was then classified as a new Galactic supernova remnant G292.2–0.5. No radio emission from a PWN was found in the ATCA data, and the observed upper limit is below what might at first be expected from the pulsar's characteristics.

Previous X-ray observations of the system were performed with the *ASCA* and *ROSAT* satellites (Pivovaroff et al. 2001). These showed extended emission associated with the radio SNR, as well as a hard point-like *ASCA* source in the field offset ~1.5′ from the radio pulsar. Such a large offset made their association uncertain. The low number of counts obtained from the SNR did not make it possible to characterize its X-ray spectral properties as thermal or nonthermal.

This new SNR/PSR system then offers a new testing ground for our current theories of the birth and evolution of these objects. For this reason, a pointed *Chandra* observation of the system was proposed for the 2001–2002 observing cycle. *Chandra*'s excellent spatial resolution and sensitivity make it the ideal observatory to look for small and faint pulsar signatures and to study the diffuse emission from surrounding material. For this thesis, a detailed analysis of the *Chandra* observation of PSR J1119–6127 and the center of the SNR

G292.2–0.5 was performed.

6.2 Observation and Data reduction

The field around pulsar J1119–6127 was observed with *Chandra* on 2002 March 31–April 1. The coordinates of the X-ray source detected with *ASCA* were positioned at the aimpoint of the back-illuminated S3 chip of the Advanced CCD Imaging Spectrometer (ACIS). The CCD temperature was -120°C with a frame readout time of 3.2 sec in "very faint" telemetry mode. The CTICORRECTIT tool was applied to the original event 1 raw data (Townsley et al. 2000) in order to correct for charge transfer inefficiency. The standard 0.5″ pixel randomization was removed. The lightcurve from source-free regions in the S3 chip were inspected and no significant background flares were found. To reduce background, only *ASCA* grades of 0, 2, 3, 4 and 6 were selected, as well as data free from bad columns and hot pixels. The resulting effective exposure time was 47 ks (~13 hrs).

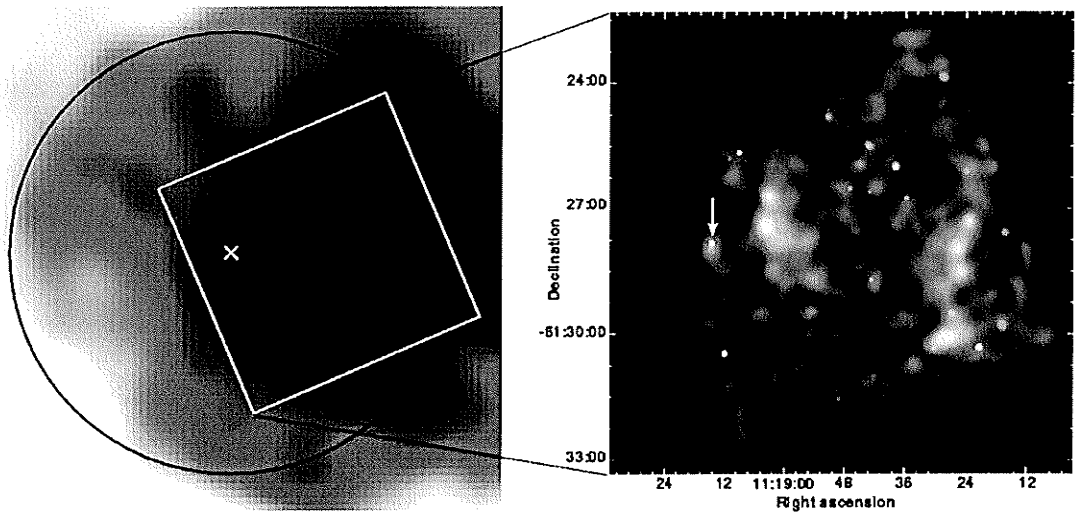

Figure 6.1: Left – 2.0–10.0 keV ASCA image of SNR G292.2–0.5. The superimposed regions mark the locations of Chandra's S3 chip (white box), the radio coordinates of PSR J1119–6127 (white cross) and the radio boundary of G292.2–0.5 (black circle, 15' diameter). Right – 0.5–10.0 keV Chandra ACIS-S3 image of the interior of the remnant. Individual images in the soft (0.5–1.15 keV, red), medium (1.15–2.3 keV, green), and hard (2.3–10.0 keV, blue) bands were combined. Resolution ranges from 1"–10" and black regions represent non-significant detection. The arrow marks the location of the detected counterpart of PSR J1119–6127 (see Section 6.3.3 for details).

Figure 6.1 shows the *ASCA* (left) and *Chandra* (right) images of G292.2–0.5. The 2.0–10.0 keV *ASCA* image has been smoothed using a Gaussian with σ = 45"[6]. The *Chandra* image was obtained as follows: the data were divided into individual images in the soft (0.5–1.15 keV, red), medium (1.15–2.3 keV, green), and hard (2.3–10.0 keV, blue) bands. Each image was adaptively smoothed using a Gaussian with σ = 1" for significance of detection >5 and up to σ = 10" for significance down to 3. A broadband (0.5–10.0 keV) background

[6] See Pivovaroff et al. (2001) for a detailed analysis of the *ASCA* data.

image was produced using the blank-sky datasets available in CALDB v2.12. The resulting background image was divided into the same energy bands and then subtracted from its corresponding (source + background) image. The individual background-subtracted images were finally combined to produce the image shown in Figure 6.1. This image shows several resolved X-ray sources surrounded by diffuse emission from the interior of the remnant.

6.3 Analysis

6.3.1 Point Sources

Point sources in the field were found using CELLDETECT, a wavelet detection algorithm implemented within CIAO. This algorithm searches for sources by summing counts in square cells ("detect" cells) in the dataset and comparing the counts to those of "background" cells. At each point where a cell is placed, a signal-to-noise ratio (S/N) of source to background counts is computed. If this ratio is above the detection threshold, a candidate source is recorded. The size of the detect cell is determined by the size of *Chandra*'s point spread function (PSF) at that location and the encircled energy percentage specified by the user. In the center of the field, the cells are small; off-axis, the cells become larger. The background count rate is estimated from a background cell which surrounds each detect cell. Since false sources may be detected in the vicinity of significant exposure variations, such as detector edges or chip gaps, an exposure map is used (a map of the total exposure time as a function of position on the CCD).

For this analysis, the S/N detection threshold was set to 2.75, the encircled energy

percentage was set to 80%, and a cutoff ratio of 95% was used for exposure variations in the field. A total of 18 sources were detected and their properties listed in *Table 6.1* in order of increasing right ascension. The number of counts was determined from the cell size used by CELLDETECT, a function of the PSF at specific off-axis angles and the encircled energy percentage. This size varied from ~1″ for the source closest to the aimpoint (s15) to ~5.5″ for the source with the largest off-axis angle (s1). For sources s17 and s18, different extraction radii were used (see below for details). With the specified S/N > 2.75, the lowest number of counts detected was 14 counts for s15. The number of counts were divided into those detected in a soft (0.5–2.0 keV) and a hard (2.0–10.0 keV) band to provide an initial indication of the X-ray spectra of these sources from the available number of counts. From this, 11 sources were found to have more that two times the number of counts in the soft band than in the hard band ("soft" sources), 4 sources have similar number of counts in both energy bands ("intermediate" sources) and 3 sources have more that two times the counts in the hard band than in the soft band ("hard" sources).

Table 6.1: Chandra catalogue of point sources detected in the field surrounding PSR J1119–6127.

ID	IAU Name (CXOU+)	Right Ascension (α_{J2000})	Declination (δ_{J2000})	Positional error (1σ, arcsec)	0.5-2.0 keV counts	2.0-10.0 keV counts
s1	J111816.8-612732	11:18:16.8	-61:27:32.1	4.2	16	8
s2	J111817.2-612945	11:18:17.2	-61:29:45.2	3.6	32	2
s3	J111821.5-613019	11:18:21.5	-61:30:19.0	3.7	34	6
s4	J111823.5-612719	11:18:23.5	-61:27:19.1	2.7	29	3
s5	J111824.2-612606	11:18:24.2	-61:26:06.1	3.2	2	35
s6	J111827.0-612929	11:18:27.0	-61:29:29.5	2.6	27	1
s7	J111828.9-612353	11:18:28.9	-61:23:53.1	4.1	32	0
s8	J111830.5-613019	11:18:30.5	-61:30:19.8	2.4	19	4
s9	J111835.9-612645	11:18:35.9	-61:26:45.6	2.3	34	2
s10	J111838.1-612600	11:18:38.1	-61:26:00.5	1.5	9	12
s11	J111842.3-613058	11:18:42.3	-61:30:58.1	1.7	5	20
s12	J111843.0-612532	11:18:43.0	-61:25:32.9	2.8	0	20
s13	J111843.2-612636	11:18:43.2	-61:26:36.6	1.8	8	15
s14	J111851.4-612449	11:18:51.4	-61:24:49.7	2.0	28	3
s15	J111905.1-612714	11:19:05.1	-61:27:14.1	0.7	9	5
s16	J111908.9-612540	11:19:08.9	-61:25:40.7	1.2	33	6
s17	J111911.8-613026	11:19:11.8	-61:30:26.7	0.8	118	13
s18	J111914.4-612749	11:19:14.4	-61:27:49.7	0.8	163	122

Various catalogues at radio, infrared, optical and X-ray wavelengths were searched in an attempt to identify the detected sources with previously known objects. Three sources were identified and are listed in Table 6.2. The soft source s3 is coincident, within error, with the

Wolf-Rayet star WR44a (α_{J2000}=11:18:43.5, δ_{J2000} = –61:26:37). The intermediate source s13 is coincident with the IRAS source J11161-6113 (α_{J2000}=11:18:22, δ_{J2000} = –61:30:19, 33″x3″ ellipse error). And finally, we have detected a source (s18) coincident with the radio pulsar J1119–6127.

From all sources detected, only two (s17 and s18) contain enough counts to extract a useful X-ray spectrum. The properties of s17 are examined below (Section 6.3.2), with those of s18 being discussed extensively (Section 6.3.3).

Table 6.2: Counterparts to detected Chandra sources.

ID	IAU Name (CXOU+)	Counterpart	Reference	Radial Offset (arcsec)
s3	J111821.5-613019	WR 44a	van der Hucht (2001)	2.3
s13	J111843.2-612636	IRAS J11161-6113	Beichman et al. (1988)	3.6
s18	J111914.4-612749	PSR J1119–6127	Camilo et al. (2000)	0.7

6.3.2 CXOU J111911.8–613026 (s17)

The *Chandra* field surrounding source CXOU J111911.8–613026 (s17) is shown in Figure 6.2. It is the second brightest source in the field, however, no counterparts at other wavelengths were found. A total of 131 counts were detected from it in the 0.5–10.0 keV range, translating into a count rate of $(2.8 \pm 0.3) \times 10^{-3}$ cts s^{-1}. The source lies at an off-axis angle of 1.7′ from the aimpoint of the S3 chip.

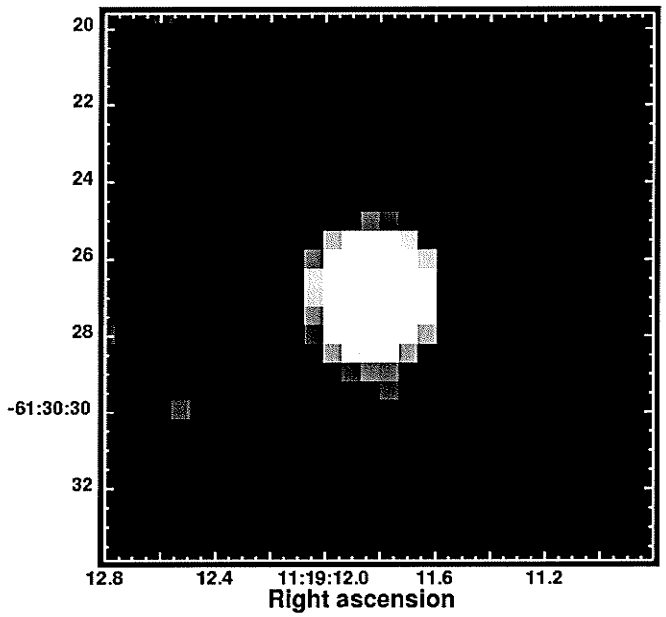

Figure 6.2: 0.5-10 keV Chandra image of the source CXOU J111911.8–613026.

In order to compare the spatial characteristics of this source with *Chandra*'s point-spread-function (PSF), a 2-D spatial fit to the data was performed using the GAUSS2D function in the *Sherpa* v2.2 software available within CIAO. From this, the measured FWHM value of ~0.9″ makes this source consistent with a point source at the observed off-axis angle. A spectrum was extracted from this source in the 0.5–10 keV band using 10 counts per energy bin. Figure 6.3 shows a plot of the spectrum and fitted model. Table 4.2 shows the parameters derived from fitting nonthermal power law and thermal bremsstrahlung models to this spectrum. The power law model provides a slightly better fit with the available number of counts than thermal models.

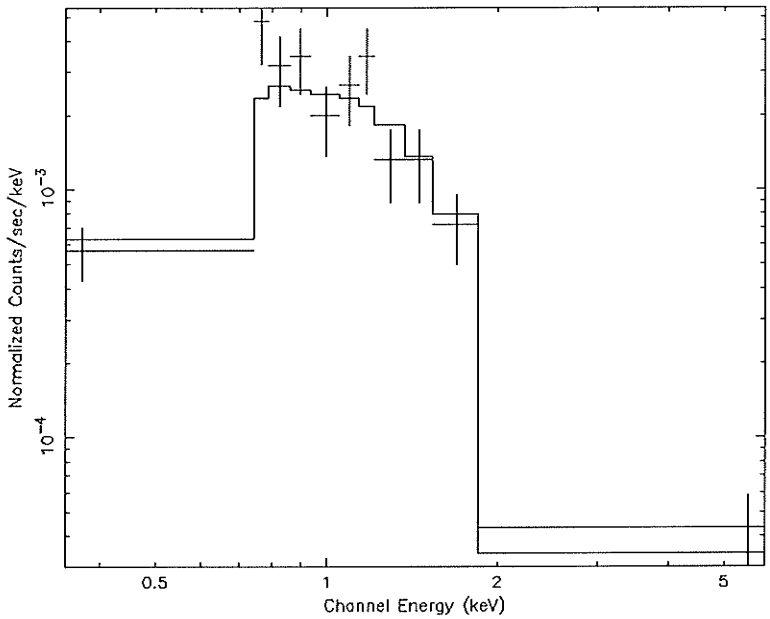

Figure 6.3: Chandra spectrum of source CXOU J111911.8–613026 with best fit power law model.

Parameter	Power law (±90%)	Thermal Brem. (±90%)
$N_H (10^{21}$ cm$^{-2})$	$5.0^{+2.0}_{-1.2}$	$3.0^{+1.6}_{-1.2}$
Γ / kT	3.9 ± 0.6	$0.75^{+0.50}_{-0.33}$ keV
Norm	$(1.3^{+1.6}_{-1.3}) \times 10^{-5}$	$(2^{+6}_{-2}) \times 10^{-5}$
$f_{abs}(0.5-10keV$, ergs cm^2 s$^{-1})$	$\left(9.2^{+2.4}_{-9.2}\right) \times 10^{-15}$	$\left(0.8^{+7.7}_{-0.8}\right) \times 10^{-14}$
$f_{unabs}(0.5-10keV$, ergs cm^2 s$^{-1})$	$\left(4.1^{+4.5}_{-4.1}\right) \times 10^{-14}$	$\left(1.8^{+11}_{-1.8}\right) \times 10^{-14}$
χ^2_v (dof)	0.76(11)	0.88(11)

Table 6.3: Parameters found from spectral fits to the source CXOU J111911.8–613026. The normalization for the power law model is given in units of photons keV^{-1} cm^{-2} s^{-1} at 1 keV, and for the bremsstrahlung model in units of $\left(3.02 \times 10^{-15} / 4\pi D^2\right) \int n_e n_i dV$ *cm^{-5}, where* D *is the distance to the source (in cm) and* n_e, n_i *are the electron and ion densities (in cm^{-3}), respectively.*

6.3.3 PSR J1119–6127

In Figure 6.4 (left) we show a close-up image of the ACIS field around the radio pulsar J1119–6127. The X-ray source s18 from *Table 6.1* is the brightest one in the field and it lies 0.7″ away from the coordinates of the radio pulsar (α_{J2000}=11:19:14.30 and δ_{J2000} = –61:27:49:5, 0.3″ error, Camilo et al. 2000). From the positional coincidence of this X-ray source with the radio pulsar, the low probability of a chance alignment ($\sim 1\times10^{-4}$), the evidence of a PWN associated with it and the nature of its spectrum (see below), this source then represents the X-ray counterpart of PSR J1119–6127.

Within a radius of 3.4″ centered at the X-ray coordinates and including the point source and extended component, a total of 285 background subtracted events were detected in the 0.5–10.0 keV band, translating to a count rate of $(6.4\pm0.4)\times10^{-3}$ cts s^{-1}. Pile-up effects are then negligible. The spectrum was fitted in the 0.5–10.0 keV band, using a minimum of 15 counts per bin. An absorbed power law model provided a better fit than thermal models. The best-fit spectral parameters are summarized in Table 6.4 and the spectrum is shown in Figure 6.4 (right). All errors are at the 90% confidence level unless otherwise specified. By examining Figure 6.4 (right), high residuals at ~1.4 keV are present, indicating that the spectrum could be partly thermal. However, these residuals become insignificant when extracting a spectrum from a smaller region. The poor statistics did not allow fitting multi-component models. A detailed investigation of this emission will have to await a deeper exposure.

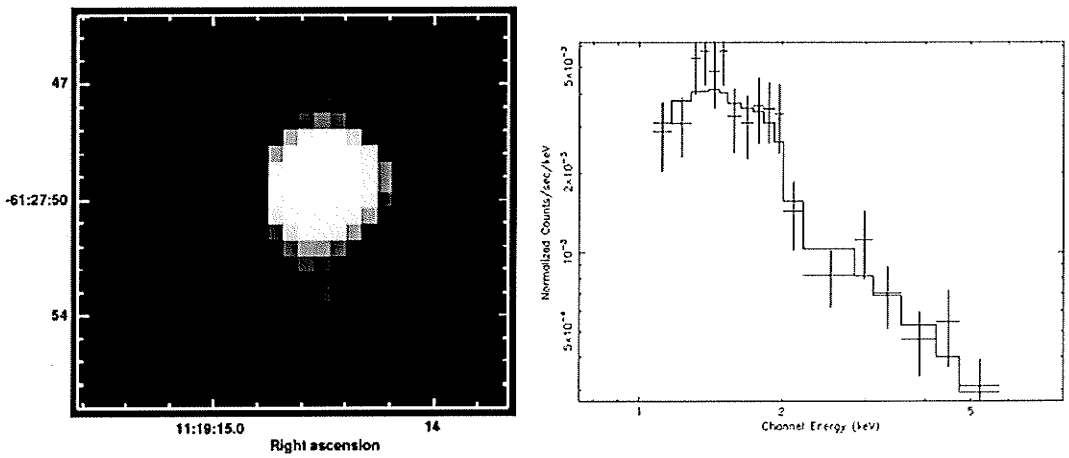

Figure 6.4: Left – The X-ray counterpart of PSR J1119–6127. This 'truecolor' image combines the soft (0.5–1.15keV, red), medium (1.15–2.15 keV, green), and hard (2.15–10 keV, blue) bands. The images were smoothed with a Gaussian with σ =0.5". Right – Spectrum and best fit power-law model (see Table 6.4). A minimum significance of 3σ was chosen in rebinning the data for display.

Parameter	Value ($\pm$ 90%)
N_H (10^{21}cm^{-2})	9^{+5}_{-3}
Photon index, Γ	$2.2^{+0.6}_{-0.3}$
Norm$_{1keV}$ (photons keV^{-1} cm^{-2} s^{-1})	$(3.1^{+3.3}_{-1.5})\times10^{-5}$
f_{abs} (0.5–10.0 keV, ergs cm^{-2} s^{-1})	$(6.6^{+13.4}_{-4.8})\times10^{-14}$
f_{unabs} (0.5–10.0 keV, ergs cm^{-2} s^{-1})	$(1.3^{+2.4}_{-0.8})\times10^{-13}$
χ^2_ν(dof)	0.57 (16)

Table 6.4: Power-law spectral fit for the counterpart of PSR J1119–6127, including point source and extended component (see Section 6.3.3 for details).

As shown in Figure 6.4 (left), the pulsar has an associated extended X-ray component aligned nearly north-south. In order to compare its spatial characteristics with *Chandra*'s

PSF, a 2-D spatial fit to the data was performed using the GAUSS2D function in *Sherpa* v2.2. First, images of the source in the soft (0.5–1.15 keV), medium (1.15–2.15 keV) and hard (2.15–10.0 keV) energy bands were created. The number of counts in these energy images was 25, 170, and 90, respectively. Corresponding normalized PSF images at an off-axis angle of 1.28′ and energies characteristic of the source's energy histogram (0.85 keV, 1.7 keV and 3.0 keV) were made and used as convolution kernels when fitting. From this fit, the low energy image yielded a FWHM value fully consistent with the PSF (~0.8″), while the medium band image had a slightly larger value (~0.9″). The hard band image was best described by an elliptical Gaussian function with FWHM of ~0.9″x1.2″, confirming the extended nature of the source. Trailing in the S3 chip can be ruled out as an origin for this feature since the read-out direction is at an angle of ~35° measured counter-clockwise from the almost north-south direction of the extended emission.

In order to further characterize the morphology of this extended emission, the above energy images were first smoothed using a Gaussian with σ = 0.5″ and then normalized. The contamination by the surrounding SNR in these images is small (<7% of total). The normalized soft image (consistent with a point source) was then subtracted from the normalized hard image. Figure 6.5 shows the resulting image, which reveals structures that appear to be consistent with torus- and jet-like features surrounding the pulsar. Such features have been observed around young rotation-powered pulsars (e.g. Lu et al. 2002) and are believed to be associated with the deposition of the pulsar's energy into its surroundings.

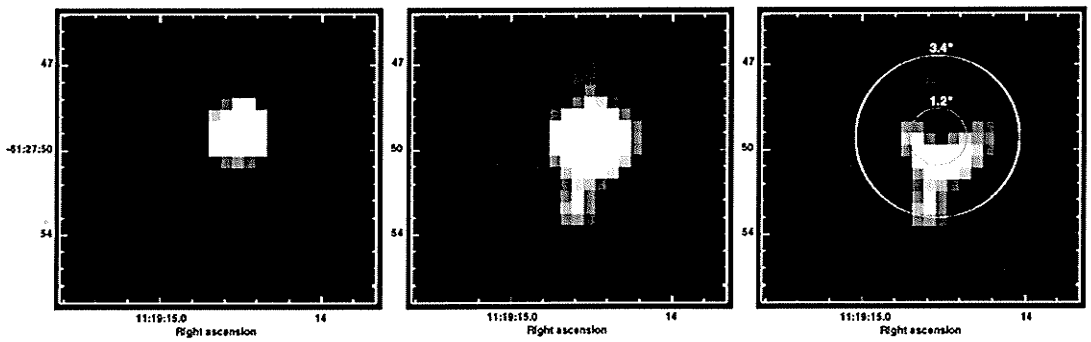

Figure 6.5: Left, Center – Normalized soft (0.5–1.15 keV, left) and hard (2.15–10.0 keV, center) energy images of PSR J1119–6127 smoothed with a Gaussian with σ = 0.5". Right – subtracting the soft (left) from the hard (center) band image makes the underlying structure surrounding the pulsar visible. A logarithmic display scale was used. See Section 6.3.3 for details.

A total of 41 background-subtracted counts were detected from an annulus centered at the X-ray coordinates with radius 1.2″–3.4″ (see Figure 6.5, right). (The inner radius was chosen to be ~1.5 times the PSF so the contamination from the point source would be less than 15%. The outer radius includes the emission detected from the extended component.) This corresponds to a significance of detection σ ~5.5 and contributes ~14% to the total count rate from the point source and extended component. From the 41 counts quoted above, 14 are present in the medium energy band (1.15–2.15 keV) and 25 in the high energy band (2.15–10.0 keV). A spectral analysis of the extended emission is not possible with the available number of counts and has to await a deeper exposure. However, unlike the point source, the extended emission is not detected in the soft band (see Figure 6.5, left). This leads one to conclude that the extended emission appears to be harder than the point source (assuming both have the same column density).

6.3.4 SNR G292.2–0.5

In order to analyze the spectral properties of the interior of G292.2–0.5, the two brightest regions of diffuse emission in the field were studied (see Figure 6.6, left). The contributions from point sources within these regions were excluded during the analysis and the north-west and south-east corners of the field were used as background. The spectral analysis was restricted to the 0.5–6.0 keV band to reduce the contamination from the background. A net of 5760 counts were detected in this range and 20 counts per energy bin were used when extracting a spectrum (see Figure 6.6, right).

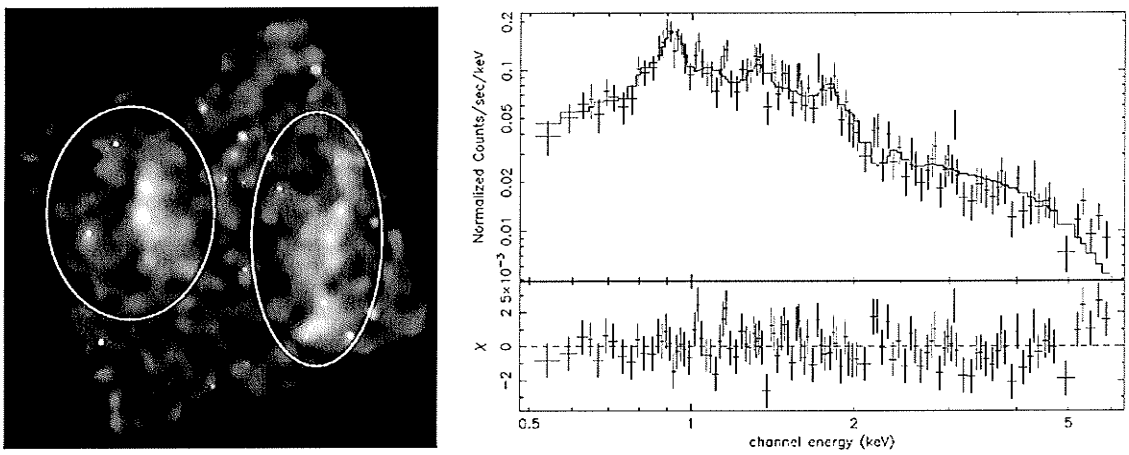

Figure 6.6: Left – Combined regions used to extract spectrum from interior of supernova remnant G292.2–0.5. Right – Spectrum obtained with best fit one-component non-equilibrium ionization model (see Table 6.5 for values).

The presence of an emission line from Neon (near 0.9 keV) indicates that the spectrum is at least partly thermal. Therefore, the data were first fitted using thermal models: CEI models

such as Raymond-Smith or Mekal, and NEI models such as VPSHOCK and VNEI (see Section 3.3). Non-equilibrium ionization (NEI) models are characterized by the shock temperature, kT, and the ionization timescale, $n_e t$, of the plasma. Here, n_e is the post-shock electron density and t is the time since the passage of the shock. The O, Ne, Mg, Si, S and Fe abundances in all models were allowed to vary independently, and the Ni abundance was tied to the Fe abundance. The NEI models were found to provide a better fit with χ^2_ν ~ 1.05(278) compared to χ^2_ν ~ 1.2(279) for the equilibrium ionization models; ν being the number of degrees of freedom.

Parameter	VPSHOCK (± 90%)
N_H (10^{21}cm^{-2})	5.8 ± 1.2
kT (keV)	36^{+40}_{-20}
O abundance$_\odot$	$0.30^{+0.30}_{-0.15}$
Ne abundance$_\odot$	$1.3^{+1.3}_{-1.0}$
Mg abundance$_\odot$	$2.1^{+3.0}_{-1.6}$
Si abundance$_\odot$	$1.3^{+0.9}_{-0.8}$
S abundance$_\odot$	$1.6^{+2.8}_{-1.6}$
Fe abundance$_\odot$	13^{+7}_{-11}
$n_e t$ (cm^{-3} s)	$(5.1^{+1.0}_{-1.5}) \times 10^9$
Norm ($10^{-14}/4\pi D^2 \int(n_e n_H \mathrm{dV})$ cm^{-5})	$(1.7 \pm 0.4) \times 10^{-3}$
f_{unabs} (0.5–10.0 keV, erg cm^{-2} s^{-1})	6.8×10^{-12}
χ^2(dof)	1.04 (278)

Table 6.5: Parameters obtained from fitting the non-equilibrium ionization model VPSHOCK to the emission from the center of G292.2–0.5.

Table 6.5 lists the values obtained from the best fit one-component VPSHOCK model. The derived values for this fit are not well constrained due to the large number of free

parameters needed to properly fit the data. The unabsorbed 0.5–10 keV flux from this fit is 6.8×10^{-12} ergs cm^{-2} s^{-1}. Although this one-component model provided a good fit to the data, a high plasma temperature of kT > 15 keV was required to properly fit the high-energy part of the spectrum. The possibility of an additional component was then explored by fitting the spectrum using various two-component models, one of them always being an NEI model. When a thermal bremsstrahlung (T.B.) or an additional NEI model were used for the second component, acceptable fits of χ^2_ν ~ 1.05 were still obtained, although high temperatures of >30 keV were also needed for this component. Therefore, a power law model was used to test for the presence of nonthermal emission from the remnant. In this case, an acceptable fit was also obtained, with a low NEI temperature in combination with a flat photon index. The values from these two-component model fits are shown in Table 6.5.

Parameter	VPSHOCK + Power law	VPSHOCK + T.B.
N_H (10^{21}cm^{-2})	3.8 ± 2.1	5.6 ± 1.6
kT (keV)	1.4 ± 1.3	0.5 ± 0.2
O abundance$_\odot$	0.2 ± 0.2	0.13 ± 0.08
Ne abundance$_\odot$	$2.1^{+3.4}_{-2.1}$	1.0 ± 0.7
Mg abundance$_\odot$	$4.1^{+7.8}_{-4.1}$	$1.9^{+2.1}_{-1.9}$
Si abundance$_\odot$	$4.8^{+12}_{-4.8}$	2.0 ± 1.9
S abundance$_\odot$	$8.7^{+20}_{-8.7}$	12^{+14}_{-12}
Fe abundance$_\odot$	$1.1^{+1.5}_{-1.1}$	$1.7^{+2.0}_{-1.7}$
$n_e t$ (cm^{-3} s)	$(5.1\pm2.0)\times10^{9}$	$(6\pm2)\times10^{9}$
$Norm_{vpshock}$	$(1.7^{+4.2}_{-1.7})\times10^{-4}$	$(1.5^{+4.3}_{-1.5})\times10^{-3}$
f_{unabs}(vpshock)	6.7×10^{-13}	1.7×10^{-12}
Γ/kT	1.1 ± 0.2	>30 keV
$Norm_{power}/Norm_{t.b.}$	$(2.3\pm0.8)\times10^{-4}$	$(8.4\pm6.0)\times10^{-4}$
f_{unabs} (Power/T.B.)	3.1×10^{-12}	2.9×10^{-12}
χ^2(dof)	1.04 (276)	1.05(276)

Table 6.6: Parameters derived from two-component (VPSHOCK + Power law) and (VPSHOCK + Thermal Bremsstrahlung) fits to the emission from G292.2–0.5. The normalization for the VPSHOCK model is given in units of $\left(10^{-14}/4\pi D^2\right)\int n_e n_H dV$ *cm*$^{-5}$, *for the power law model in units of photons keV*$^{-1}$ *cm*$^{-2}$ *s*$^{-1}$ *at 1 keV and for the thermal bremsstrahlung model in units of* $\left(3.02\times10^{-15}/4\pi D^2\right)\int n_e n_i dV$ *cm*$^{-5}$. *The unabsorbed fluxes are given in the 0.5–10.0 keV range and in units of ergs cm*$^{-2}$ *s*$^{-1}$. *Errors were calculated by allowing 10 out of the 12 fitted parameters to vary freely.*

6.4 Discussion

6.4.1 CXOU J111911.8–613026

A first approximation of the distance to this source can be made from the measured column density, N_H, as follows (see Section 5.5.1): the extinction per unit distance can be estimated from Lucke (1978) to be $E_{B-V}/D \sim 0.2$ mag kpc^{-1} and using the relation

$N_H / E_{B-V} = 5.5 \times 10^{21}$ cm^{-2} mag^{-1}, the distance D can be then be estimated. From Table 6.3, an average N_H value of $\left(4^{+3.0}_{-2.2}\right) \times 10^{21}$ cm^{-2} translates into a distance of $3.6^{+2.7}_{-2.0}$ kpc.

The source exhibits a soft spectrum, with a steep power law providing a slightly better fit than low temperature thermal models. The power law photon index of $\Gamma = 3.9 \pm 0.6$ is much steeper than those commonly exhibited by radio pulsars (Γ~2). However, it is consistent with those typically found for anomalous X-ray pulsars (AXPs, indices of $\Gamma \sim 3-5$). The unabsorbed 0.5–10 keV luminosity from the power law model is $\left(0.6^{+3.5}_{-0.6}\right) \times 10^{32}$ ergs s^{-1} after all errors have been taken into account. The source's luminosity is then well below that of AXPs (~10^{35}–10^{36} ergs s^{-1}). In addition, its overall spectral characteristics are not consistent with those of observed accretion-powered binary systems, which exhibit much higher luminosities (~10^{36}–10^{38} ergs s^{-1}) and different spectral properties.

The class of Compact Central Objects (CCOs), presumably neutron stars typified by the central object in the SNR Cas A, exhibit blackbody spectra ($kT \sim 0.3-0.6$ keV) together with steep power law indices ($\Gamma \sim 4-5$, where they fit the data) and luminosities of ~10^{33}–10^{35} ergs s^{-1} (Pavlov et al. 2001). It is then possible that source J111911.8–613026 belongs to this class of objects. However, a simple blackbody model (acceptable for most CCOs) did not result in a better fit for this source than power law or bremsstrahlung models, giving $\chi^2_\nu(dof) \sim 1.1(11)$. The known CCOs also lie near the center of SNRs, as opposed to this object which is not associated with a SNR. Thus, the nature of this source cannot be immediately determined with the available data and has to await further observations.

6.4.2 Distance to G292.2–0.5/J1119–6127

Following the same method used in Section 6.4.1, the derived values for N_H from the pulsar and remnant fits can be used to obtain a distance to the system. From the power law fit to PSR J1119–6127, the column density is $N_H = (6.0-14)\times10^{21}$ cm^{-2} (see Table 6.4). From the best fit one-component model to G292.2–0.5, the column density is $N_H = (5.0-7.0)\times10^{21}$ cm^{-2} (see Table 6.5). These then translate into a distance of 5.4–12.6 kpc for the pulsar and 4.0–6.3 kpc for the remnant. A distance of 4–8 kpc was then adopted for the system. The upper limit was determined from the location of the source with respect to the Carina spiral arm (Camilo et al. 2000).

6.4.3 PSR J1119–6127

The analysis described in Section 6.3.3 allowed us to identify the X-ray counterpart of PSR J1119–6127 and its PWN. Using the spectral model outlined in Table 6.4, we derive an unabsorbed 0.5–10.0 keV X-ray luminosity for the point source and PWN of $L_X = \left(5.5^{+10}_{-3.3}\right)\times10^{32} D_6^2$ erg s^{-1} where D_6 is the distance in units of 6 kpc. The conversion efficiency of $\dot{E}$ into L_X is then $\varepsilon_{psr+pwn} = \left(L_X / \dot{E}\right) \sim \left(2.4^{+4.5}_{-1.5}\right)\times10^{-4} D_6^2$. This value is somewhat on the low end of the efficiencies exhibited by other pulsars associated with SNRs (e.g. Safi-Harb 2002).

Table 6.7 summarizes the properties of J1119–6127 and two other pulsars with similar spin properties. PSR J1846–0258 lies within 1′ of the center of SNR Kes 75 and PSR

B1509–58 lies close to the center of SNR G320.4–1.2. All three pulsars spin slowly (P >100 ms) and have large inferred magnetic fields ($B > 1\times10^{13}$ G) compared to other young, Crab-like pulsars. However, their observed X-ray properties are different from those of J1119–6127. While PSR J1846–0258 exhibits the highest X-ray efficiency (even when compared to all other Crab-like pulsars, it has one of the highest ε values), J1119–6127 exhibits the lowest value ($\varepsilon_{psr+pwn} \leq 0.001$, using the upper limits on the luminosity and distance). Furthermore, both J1846–0258 and B1509–58 exhibit very similar spectral properties, with the measured photon indices of the X-ray pulsars being flatter than those of their associated PWNe. On the other hand, as noted above, the present analysis of PSR J1119–6127 suggests the opposite trend, with the photon index of the point source being steeper than that of the extended feature (again, these values should be taken with caution since this conclusion is based on the small number of counts available).

Therefore, it seems that the peculiar spin properties and high magnetic fields of these three pulsars cannot account in an obvious way for the differences in their X-ray properties. In addition, the extent to which their environment comes into play in explaining these differences is made uncertain by the fact that the emission from Kes 75 (Helfand et al. 2003) surrounding J1846–0258 was found to have very similar properties to those found for G292.2–0.5 in this analysis but arising from different mechanisms (see Section 6.4.4).

Parameter	J1119–6127	J1846–0258	B1509–58
Spin period, P (ms)	408	324	150
Period derivative, $\dot{P}$	4×10^{-12}	7.1×10^{-12}	1.5×10^{-12}
Surface magnetic field, B (G)	4.1×10^{13}	4.8×10^{13}	1.5×10^{13}
Characteristic age, τ_c (yr)	1600	980–1700	1700
Spin-down luminosity, $\dot{E}$ (erg s^{-1})	2.3×10^{36}	7.9×10^{36}	18×10^{36}
Braking index, n	2.91	1.86–2.48	2.8
Distance	~6 kpc	~19 kpc	~5 kpc
N_H (10^{22} cm^{-2})	~0.9	~4	~1
Photon index	$\Gamma_{psr}\gtrsim2.2$, $\Gamma_{pwn}\lesssim2.2$	$\Gamma_{psr}\sim1.4$, $\Gamma_{pwn}\sim1.9$	$\Gamma_{psr}\sim1.4$(?), $\Gamma_{pwn}\sim2.05$
Radio/X-ray PWN?	no / yes	yes / yes	yes / yes
0.5–10.0 keV efficiency, ϵ ($L_X/\dot{E}$)	$\epsilon_{psr+pwn}\lesssim0.001$	$\epsilon_{psr}\sim0.016$, $\epsilon_{pwn}\sim0.065$	$\epsilon_{psr}>0.001$, $\epsilon_{pwn}\sim0.009$
Reference	this work	Helfand et al. 2003	Gaensler et al. 2002

Table 6.7: Observed parameters for pulsars J1119–6127, J1846–0258 and B1509–58.

6.4.4 G292.2–0.5

The emission from G292.2–0.5 is well described by non-equilibrium ionization models, as is expected from young SNRs. However, the measured temperature of >15 keV is much higher than the few keV temperatures commonly observed in these objects. In addition, the low ionization timescale ($n_e t \sim 5\times10^9$ cm^{-3} s) indicates that the plasma is far from ionization equilibrium ($n_e t \sim 1\times10^{12}$ cm^{-3} s), as is expected from young remnants where the plasma has been recently ionized by the forward and reverse shocks. Unfortunately, the elemental abundances are not well constrained, making it hard to determine whether the emission arises from shocked ISM (abundances < 1 solar) or from shocked ejecta (abundances > 1 solar).

The high thermal temperatures derived from the above one-component models may be suggestive that the spectrum could be nonthermal. For remnants that exhibit both thermal

and nonthermal emission, the nonthermal portion is well described by a steep power law. Examples include Cas A ($\Gamma = 3.0 \pm 0.2$), SN 1006 ($\Gamma = 3.0 \pm 0.2$), Kepler ($\Gamma = 3.0 \pm 0.2$), Tycho ($\Gamma = 3.2 \pm 0.1$) and RCW 86 ($\Gamma = 3.3 \pm 0.2$) (Allen et al. 1999). One exception is the SNR G347.3–0.5, which lacks thermal emission down to very low limits and its nonthermal photon index is harder ($\Gamma \sim 2.2$) than those of the above remnants (Slane et al. 1999). This nonthermal emission is commonly attributed to synchrotron emission from particles accelerated at the supernova blast wave shock. In addition, flat power law photon indices of ~1.45–2.0 were derived for the SNR W50 associated with the Galactic microquasar SS 433. In this case, the emission was interpreted as arising from the interaction of fast moving jets, produced by SS 433, with the SNR shell and its surroundings (Safi-Harb & Petre 1999). However, when a thermal plus nonthermal model was fitted to the *Chandra* data of G292.2–0.5, the measured nonthermal photon index of $\Gamma \sim 1$ (see Table 6.6) is distinctly harder than those quoted above.

If the hard emission represents power law emission from relativistic electrons, the possibility then exists that they arise from a leakage of PWN particles into the SNR interior. The observed photon index for this extended emission also agrees with the suggested index for the PWN of $\Gamma < 2.2$, indicating they might have a similar origin. In this case, the particles would have had to travel from the location of the PWN out to a radius of ~6′ (the location of the outer region selected to study the emission from G292.0+1.8, see Figure 6.6). The synchrotron lifetime of these particles must then exceed the light travel time for this distance, $\tau_{synch} > r/c \sim (0.7-1.4)\times 10^9 s$ ~ 23–46 yrs (at distances of 4–8 kpc). The contribution from the power law component to the overall spectrum is still very significant (in fact, it

dominates) at energies E ~6 keV (for example). The SNR magnetic field needed to produce the synchrotron emission at these energies with the above lifetime can then be estimated as B_{snr} <$0.85\,\tau_{synch,yrs}^{-2/3}\,E_{keV}^{-1/3}$ G ~$(0.5-1.5)\times10^{-4}$ G (Lang 1999). This is higher than the typical interstellar magnetic field of a few μ G.

Interestingly, the emission from the SNR Kes 75 associated with the high magnetic field pulsar J1846–0258 was also found to have a similar nonthermal component with $\Gamma = 1.34 \pm 0.14$ (Helfand et al. 2003). In this case, Helfand et al. concluded that the emission is not likely to arise from pulsar-injected particles and they instead suggested a dust-scattering halo of the PWN as its origin. However, this process could not completely account for the high energy (4–7 keV) power law contribution to the spectrum and a synchrotron contribution from the SNR with unusually flat index cannot be ruled out in this case. Additional analysis of both these remnants will make it possible to further constrain their properties and determine possible similarities in their emission mechanisms.

Chapter 7

Conclusions

In this thesis, the high resolution and sensitivity of the *Chandra X-ray Observatory* were exploited to make unique observations of the Galactic supernova remnants, G292.0+1.8 and G292.2–0.5. The imaging and spectral capabilities offered by *Chandra* were used to derive basic properties of these objects.

The emission from the composite remnant G292.0+1.8 was found to arise predominantly from ejecta-dominated regions. Fitting nonequilibrium ionization (NEI) models to this emission allowed for the identification of the supernova blast wave. A progenitor mass of 30–40 $M_{\odot}$ was derived by comparing the derived abundances from the ejecta with those predicted from nucleosynthesis models. Using the Sedov interpretation, the explosion energy, age, blast wave velocity and swept-up mass of the remnant were found to be $\left(1.8^{+0.8}_{-0.6}\right)\times 10^{50}$ ergs, $2,600^{+250}_{-200}$ yrs, 880 ± 70 km s^{-1} and $15.6^{+4.5}_{-3.5}$ $M_{\odot}$, respectively. The derived age is almost twice as large as previous estimates and it is close to the pulsar's characteristic age of 2,900 yrs. This confirms their association and relaxes the need for the pulsar to have a value for the braking index different than $n = 3$, a large period at birth or a high transverse velocity. The properties of the pulsar wind nebula surrounding PSR J1124–5916 were also studied. A steepening of the PWN power law photon index from $\Gamma = 2.0 \pm 0.1$ to $\Gamma = 3.0 \pm 0.2$ with increasing radius was found, as expected from

synchrotron and expansion losses. From the Kennel & Coroniti (1984a) model, it was found that the PWN is consistent with having a shock radius of a few arcseconds and a magnetization parameter $\sigma \sim 0.0005 - 0.01$.

The *Chandra* observation of the remnant G292.2–0.5 allowed for the detection of the X-ray counterpart of the high-magnetic field radio pulsar J1119–6127. In addition, a faint 3″x6″ extended component surrounding the pulsar was identified at energies above ~1.2 keV representing the first evidence for a PWN. The combined emission from the pulsar and its PWN was well described by a power law with a photon index $\Gamma = 2.2^{+0.6}_{-0.3}$ and unabsorbed 0.5–10 keV luminosity of $\left(5.5^{+10}_{-3.3}\right)\times 10^{32}$ ergs s^{-1} at a distance of 6 kpc. The emission from the interior of the SNR was well described by both a single NEI model with high temperatures (kT > 15 keV) or a two-component NEI plus power law model with an unusually flat photon index (kT ~ 1.5 keV and Γ ~ 1.1). In the case where the hard SNR emission represents synchrotron radiation from relativistic electrons supplied by the PWN, a magnetic field of $\sim\left(0.5-1.5\right)\times 10^{-4}$ G is needed inside the remnant to produce the observed emission.

From the above results, these two remnants appear to exhibit different properties. G292.0+1.8 can be considered a textbook case for a composite remnant, where both thermal emission from the extended regions and nonthermal emission from the pulsar/PWN are present. The thermal emission is dominated by high abundance ejecta and is consistent with a massive progenitor. With this study, the derived age for the remnant is similar to the

characteristic age of the pulsar. In addition, the emission from the PWN follows the steepening trend expected from synchrotron loses. On the other hand, from this study it now seems that G292.2–0.5 provides complications with the traditional picture of a young, composite SNR. The emission from the interior is either hotter than that of other thermal remnants, or much flatter than that of other nonthermal remnants. In addition, even though a PWN was detected surrounding PSR J1119–6127, as expected from its youth, it does not seem to be Crab-like, most probably due to the pulsar's high magnetic field. Furthermore, the PWN appears to have an unusually low luminosity and a flatter spectral index than the pulsar, in contrast to what is observed for other high-magnetic field pulsars.

These remnants and their compact objects then exhibit different properties and represent two distinct manifestations of the SNR/PSR systems. Additional high resolution *Chandra* observations of these systems, and in particular of G292.2–0.5/J1119–6127, will allow for a more reliable determination of the spatial and spectral characteristics of their arcsecond-scale structures associated with the deposition of the pulsar wind's energy into its surroundings. Furthermore, future observations with the *XMM-Newton* X-ray satellite will provide a large effective area and sensitivity to low-surface brightness structures, such as jet-like structures and SNR filaments. X-ray observations, complimented with studies at other wavelengths, will provide a better understanding of a wide range of PSR/SNR systems and the role played by the progenitor stars and the ambient medium in determining their properties. Thus, the studies carried out for this thesis illustrate the need to increase our sample of these systems in order to broaden our understanding of them.

Appendix A

Nonequilibrium Ionization Fits to G292.0+1.8

Tables A.1 and A.2 show the best-fit one- and two-component nonequilibrium (NEI) models to the 23 regions selected for spatially resolved spectroscopy in the remnant G292.0+1.8 (see Figure 5.4). The NEI model VPSHOCK was used to describe the spectra. The normalization (Norm) in these tables is given in units of $\left(10^{-14}/4\pi D^2\right)\int n_e n_H dV\ cm^{-5}$. The listed values were used to derive overall parameters for the remnant. See Table 5.3 and Table 5.4 for errors of individual values that were used during analysis.

Table A.1: One-component VPSHOCK fits to the 23 regions selected for spatially resolved spectroscopy in the remnant G292.0+1.8.

Parameter	region 1	region 2	region 3	region 4	region 5	region 6
$N_H\ (10^{21}\ cm^{-2})$	4.5	5.4	3.2	5.2	4.9	2.7
$kT\ (keV)$	0.75	1.7	0.76	1.5	0.64	0.64
O abundance$_\odot$	5.3	2.5	2.5	1.3	6.0	1.5
Ne abundance$_\odot$	6.3	6.6	3.9	1.9	6.1	2.0
Mg abundance$_\odot$	3.7	3.8	2.5	1.3	3.0	1.6
Si abundance$_\odot$	0.7	0.9	0.3	0.3	2.4	0.9
S abundance$_\odot$	0.9	0.5	0.5	0.2	5.0	1.6
Fe abundance$_\odot$	0.7	0.1	0.6	0.3	0.9	1.6
$n_e t\ (cm^{-3}\ s)$	5.7×10^{11}	4.4×10^{11}	6.9×10^{11}	1.5×10^{11}	1.9×10^{12}	5×10^{10}
Norm (10^{-3})	1.3	0.39	1.2	1.4	3.4	6.4
$\chi_\nu^2(dof)$	1.97(118)	1.74(93)	1.77(107)	1.61(125)	2.50(152)	2.76(176)

Table A.1: One-component fits continued

Parameter	region 7	region 8	region 9	region 10	region 11	region 12
$N_H\ (10^{21}\ cm^{-2})$	2.7	3.7	0.26	4.0	3.5	4.4
$kT\ (keV)$	0.56	0.56	0.69	0.62	1.2	0.77
O abundance$_\odot$	1.4	0.9	2.2	3.2	1.1	0.8
Ne abundance$_\odot$	1.4	0.8	10	3.1	3.0	1.1
Mg abundance$_\odot$	1.0	0.6	3.7	1.8	2.3	0.8
Si abundance$_\odot$	1.2	0.8	0.6	1.0	1.1	0.6
S abundance$_\odot$	3.3	1.4	1.0	1.8	0.9	1.1
Fe abundance$_\odot$	0.5	0.4	0.3	0.7	0.2	0.2
$n_e t\ (cm^{-3}\ s)$	3.7×10^{13}	2.7×10^{12}	1.0×10^{13}	1.2×10^{12}	3.3×10^{11}	3.0×10^{11}
Norm (10^{-3})	0.58	6.6	1.0	3.5	0.33	2.0
$\chi^2_\nu(dof)$	1.07(112)	1.02(180)	2.16(120)	1.47(147)	1.13(115)	1.85(107)

Parameter	region 13	region 14	region 15	region 16	region 17	region 18
$N_H\ (10^{21}\ cm^{-2})$	5.0	5.4	5.7	4.9	3.9	4.9
$kT\ (keV)$	0.81	0.89	0.92	0.78	0.92	0.95
O abundance$_\odot$	5.6	4.4	4.2	3.6	1.8	2.9
Ne abundance$_\odot$	6.2	5.7	6.7	4.5	3.4	3.2
Mg abundance$_\odot$	3.3	2.9	3.6	2.2	2.2	2.2
Si abundance$_\odot$	1.1	0.5	0.9	2.6	0.8	0.4
S abundance$_\odot$	1.0	0	1.5	2.4	0.7	0.8
Fe abundance$_\odot$	0.8	0.5	0.3	0.3	0.5	0.5
$n_e t\ (cm^{-3}\ s)$	4.7×10^{11}	3.4×10^{11}	3.5×10^{11}	7.3×10^{11}	2.1×10^{11}	3.7×10^{11}
Norm (10^{-3})	1.3	0.77	1.4	0.66	0.43	1.3
$\chi^2_\nu(dof)$	2.05(117)	1.79(105)	1.44(142)	1.24(118)	1.15(109)	1.93(113)

Table A.1: One-component fits continued

Parameter	region 19	region 20	region 21	region 22	region 23
$N_H\ (10^{21}\ cm^{-2})$	4.4	4.7	4.9	3.5	3.1
$kT\ (keV)$	0.71	0.66	0.87	0.70	0.72
O abundance$_\odot$	2.0	1.1	0.4	0.5	0.3
Ne abundance$_\odot$	5.7	0.9	0.5	0.5	0.4
Mg abundance$_\odot$	1.7	0.6	0.2	0.3	0.1
Si abundance$_\odot$	0.6	0.5	0.3	0.2	0.2
S abundance$_\odot$	1.3	1.2	0.2	0.7	0.5
Fe abundance$_\odot$	0.1	0.2	0.2	0.1	0
$n_e t\ (cm^{-3}\ s)$	4.7×10^{12}	7.5×10^{11}	8.7×10^{10}	4.0×10^{11}	4.6×10^{11}
Norm (10^{-3})	0.96	3.3	1.4	0.92	2.2
$\chi^2_\nu(dof)$	1.09(94)	1.9(112)	1.16(98)	1.33(90)	1.40(112)

Table A.2: Two-component VPSHOCK fits to the first 21 regions selected for analysis in G292.0+1.8.

Parameter	region 1	region 2	region 3	region 4	region 5	region 6
$N_H\ (10^{21}\ cm^{-2})$	4.9	6.8	7.0	5.9	6.0	4.7
$kT_{hot}\ (keV)$	0.85	1.8	0.90	1.9	0.74	1.2
$n_e t_{hot}(cm^{-3}\ s)$	4.8×10^{11}	2.7×10^{11}	3.2×10^{11}	2.0×10^{11}	8.0×10^{11}	1.0×10^{11}
$Norm_{hot}(10^{-3})$	1.5	0.4	0.9	0.9	4.1	5.9
$kT_{cool}\ (keV)$	0.24	0.32	0.16	0.39	0.2	0.24
$n_e t_{cool}(cm^{-3}\ s)$	4.4×10^{13}	1.1×10^{9}	1.4×10^{13}	4.9×10^{11}	3.0×10^{12}	7.0×10^{11}
$Norm_{hot}(10^{-3})$	1.9	1.4	2.6	0.8	5.8	7.9
$\chi^2_\nu(dof)$	1.76(109)	1.84(84)	1.31(104)	1.35(116)	1.64(139)	2.34(169)

Table A.2: Two-component fits continued

Parameter	region 7	region 8	region 9	region 10	region 11	region 12
$N_H\ (10^{21}\ cm^{-2})$	4.1	4.4	2.7	5.2	5.6	6.3
$kT_{hot}\ (keV)$	1.3	0.58	0.80	0.70	1.2	0.82
$n_e t_{hot} (cm^{-3}\ s)$	9.4 x 10^{10}	6.2 x 10^{12}	6.7 x 10^{12}	1.1 x 10^{12}	2.8 x 10^{11}	5.3 x 10^{11}
$Norm_{hot} (10^{-3})$	1.6	3.5	0.5	2.6	0.3	0.9
$kT_{cool}\ (keV)$	0.49	0.49	0.42	0.24	0.13	0.42
$n_e t_{cool} (cm^{-3}\ s)$	5.0 x 10^{13}	8.7 x 10^{9}	1.5 x 10^{10}	4.3 x 10^{12}	8.6 x 10^{11}	5.0 x 10^{10}
$Norm_{hot} (10^{-3})$	0.4	0.8	0.03	7.9	1.0	1.2
$\chi_v^2 (dof)$	1.16(103)	0.97(171)	1.71(111)	1.13(140)	1.20(106)	1.33(98)

Parameter	region 13	region 14	region 15	region 16	region 17	region 18
$N_H\ (10^{21}\ cm^{-2})$	6.0	4.8	6.8	4.9	4.5	4.8
$kT_{hot}\ (keV)$	0.86	0.89	0.95	1.1	0.92	1.1
$n_e t_{hot} (cm^{-3}\ s)$	6.6 x 10^{11}	4.4 x 10^{11}	5.4 x 10^{11}	3.1 x 10^{11}	2.4 x 10^{11}	3.1 x 10^{11}
$Norm_{hot} (10^{-3})$	1.6	0.7	1.2	0.3	0.5	0.9
$kT_{cool}\ (keV)$	0.41	0.38	0.37	0.32	0.27	0.65
$n_e t_{cool} (cm^{-3}\ s)$	2.5 x 10^{11}	4.4 x 10^{13}	4.9 x 10^{11}	8.3 x 10^{8}	1.2 x 10^{10}	3.0 x 10^{10}
$Norm_{hot} (10^{-3})$	1.7	0.1	3.3	1.6	1.4	0.3
$\chi_v^2 (dof)$	1.62(109)	1.72(97)	1.43(133)	1.15(109)	1.12(100)	1.63(105)

Table A.2: Two-component fits continued

Parameter	region 19	region 20	region 21
$N_H\ (10^{21}\ cm^{-2})$	5.5	6.1	6.1
$kT_{hot}\ (keV)$	1.4	0.94	0.95
$n_e t_{hot} (cm^{-3}\ s)$	2.7 x 10^{11}	3.0 x 10^{11}	5.9 x 10^{9}
$Norm_{hot} (10^{-3})$	0.2	1.1	0.9
$kT_{cool}\ (keV)$	0.48	0.27	0.84
$n_e t_{cool} (cm^{-3}\ s)$	8.5 x 10^{8}	2.7 x 10^{11}	1.4 x 10^{11}
$Norm_{hot} (10^{-3})$	0.8	5.1	0.3
$\chi_v^2 (dof)$	1.10(84)	1.62(109)	1.05(95)

Publications

Summarized versions of the results presented in this thesis have been previously published in the following articles:

Gonzalez, M. E. & Safi-Harb, S., "*Chandra* Detection of the High-Magnetic Field Radio Pulsar J1119–6127 in the Supernova Remnant G292.2–0.5", *Astrophysical Journal Letters*, v.591, p.143, 2003

Gonzalez, M. E. & Safi-Harb, S., "New Constraints of the Energetics, Progenitor Mass, and Age of the Supernova Remnant G292.0+1.8 Containing PSR J1124–5916", *Astrophysical Journal Letters*, v.583, p.91, 2003.

Safi-Harb, S. & Gonzalez, M. E., "*Chandra* Observations of the Oxygen-rich Supernova Remnant MSH 11–54 (G292.0+1.8)", in ASP Conf. Ser. 262, The High Energy Universe at Sharp Focus: *Chandra* Science, ed. E. M. Schlegel & S. B. Vrtilek (San Francisco: ASP), p.315, 2002

Abbreviations

The following is a list of the common abbreviations found throughout this thesis.

ACIS	Advance CCD Imaging Spectrometer; detector on *Chandra*
ASCA	Advanced Satellite for Cosmology and Astronomy; X-ray telescope
BI	Back-illuminated CCD
CALDB	Calibration Database; *Chandra* calibration files directory
CCD	Charge Coupled Device
CHANDRA	Chandra X-ray Observatory (or CXO); X-ray satellite
CIAO	Chandra Interactive Analysis of Observations
CIE	Collision Ionization Equilibrium
CXC	Chandra X-ray Center
FI	Front-illuminated CCD
FPCS	Focal Plane Crystal Spectrometer; detector on *Einstein* observatory
FWHM	Full-width at Half Maximum
GIS	Gas Imaging Spectrometer; detector on *ASCA*
HPD	Half-power Diameter
HRC	High Resolution Camera; detector on *Chandra and Einstein* observatories
HRI	High Resolution Imager; detector on *ROSAT*
HRMA	High Resolution Mirror Assembly; mirrors on *Chandra*
ISM	Interstellar Medium
IPC	Imaging Proportional Counter; detector on *Einstein* observatory
NEI	Nonequilibrium Ionization
PSPC	Position Sensitive Proportional Counter; detector on *ROSAT*
PSF	Point Spread Function
PSR	Pulsar
PWN	Pulsar Wind Nebula
ROSAT	Röentgensatellit; X-ray satellite
SIS	Solid-state Imaging Spectrometer; detector on *ASCA*
SNR	Supernova Remnant

Bibliography

Allen, G. E., Petre, R. & Gotthelf, E. V. 2001, ApJ, 558, 739

Anders, E. & Grevesse, N. 1989, GeCoA, 53, 197

Arnaud, K.A. 1996, Astronomical Data Analysis Software and Systems V, ASP Conference Series, Vol. 101, 1996, Eds. G.H. Jacoby and J. Barnes, p. 17.

Arnaud, M. & Rothenflug, R. 1985, A&A Suppl, 60, 425

Beichman, C.A., Neugebauer, G., Habing, H.J., Clegg, P.E., & Chester T.J. 1988, NASAR, 1190, 1

Blondin, J. M., Wright, E. B., Borkowski, K J. & Reynolds, S. P. 1998, ApJ, 500, 342

Borkowski, K.J., Lyerly, W.J., & Reynolds, S.P. 2001, ApJ, 548, 820

Camilo, F., Kaspi, V. M., Lyne, A. G., Manchester, R. N., Bell, J. F., D'Amico, N., McKay, N. P. F., & Crawford, F. 2000, ApJ, 541, 367

Camilo, F., Manchester, R. N., Gaensler, B. M., Lorimer, D. R., & Sarkissian, J. 2002a, ApJ, 567, 71

Cioffi, D. F. 1990, Physical Processes in Hot Cosmic Plasma, Proc. of the NATO Advanced Research Workshop, eds. Wolfgang Brickmann, Andrew Fabian, Franco Giovannelli, Kluwer Academic Publishers, Dordrecht.

Crawford, F, Gaensler, B. M., Kaspi, V. M., Manchester, R. N., Camilo, F., Lyne, A. G., & Pivovaroff, M. J. 2001, ApJ, 554, 152

Gaensler, B. M. & Wallace, B. J. 2003, ApJ, accepted, astro-ph/0305168

Gaensler, B. M., Arons, J., Kaspi, V. M., Pivovaroff, M. J., Kawal, N., & Tamura, K. 2002, ApJ, 569, 878

Green, D. A. 2001. "A Catalogue of Galactic Supernova Remnants (2001 December version)". Mullard Radio Astronomy Observatory, Cavendish Laboratory, Cambridge, UK

(http://www.mrao.cam.ac.ul/surveys/srns)

Gorenstein, P. 1977, in X-ray Astronomy, eds. Giacconi R. and Gursky H., D. Reidel Publishing Company, Holland

Hamilton, A. J., Sarazin, C. L, & Chevalier, R. A. 1983, ApJS, 51, 115

Helfand, D. J., Collins, B. F., & Gotthelf, E. V. 2003, ApJ, 582, 783

Helfand, D. J., Gotthelf, E. V., & Halpern, J. P. 2001, ApJ, 556, 380

Hughes, J. P., & Singh, K. P. 1994, ApJ, 422, 126

Hughes, J. P., Slane, P. O., Burrows, D. N., Garmire, G. P., Nousek, J. A., Olbert, C. M., & Keohane, J. W. 2001, ApJ, 559, 153

Hwang, U., Holt, S., & Petre, R. 2001, ApJ, 537, 110

Kaastra, J. S. & Bleeker, J. A. M 1991, in Iron Line Diagnostic in X-ray Sources, eds. A. Treves, G. C. Perola and L. Stella, published by Springer-Verlag, Berlin

Katz, J. I. 1987, *High Energy Astrophysics,* Addison-Wesley, California

Kennel, C. F., & Coroniti, F. V. 1984a, ApJ, 283, 694

Kennel, C. F., & Coroniti, F. V. 1984b, ApJ, 283, 710

Koyama, K., Petre, R., Gotthelf, E. V., Hwang, U., Matsura, M., Ozaki, M., & Holt, S. S. 1995, Nature, 378, 255

Lang, K. R. 1999, *Astrophysical Formulae*, Springer-Verlag, New York

Liedahl, D. A. 1999, in X-ray Spectroscopy in Astrophysics, eds. Jan van Paradijs and Johan A. M. Bleeker, published by Springer-Verlag, Berlin

Lu, F. J., Wang, Q. D., Aschenbach, B., Durouchoux, P., & Song, L. M. 2002, ApJ, 568, 49

Lucke, P. B. 1978, A&A, 64, 367

Lyne, A. G., & Lorimer, D. R. 1994, Nature, 369, L127

Manchester, R. N. & Taylor, J. H. 1977, *Pulsars,* W. H. Freeman and Company, San

Francisco

McKee, C. F. & Ostriker, J. P. 1977, ApJ, 218, 148

McKee, C. F. 1974, ApJ, 188, 335

Mewe, R. 1999, in X-ray Spectroscopy in Astrophysics, eds. Jan van Paradijs and Johan A. M. Bleeker, published by Springer-Verlag, Berlin

Masai, K. 1994, ApJ, 437, 770

Milne, D. K. 1969, Australian J. Phys., 22, 613

Murdin, P., & Clark, D. H. 1979, MNRAS, 189, 501

Park, S., Roming, P. W. A., Hughes, J. P., Slane, P. O., Burrows, D. N., Garmire, G. P., & Nousek, J. A. 2002, ApJ, 564, 39

Pavlov, G. G., Sanwal, D., Garmire, G. P., & Zavlin, V. E. 2001; astro-ph/0112322

Pedlar, A., Muxlow, T. W. B., Garrett, M. A., Diamond, P., Wills, K. A., Wilkinson, P. N. & Alef, W., 1999, MNRAS, 307, 761

Pivovaroff, M. J. 2000, Ph.D. thesis, MIT

Pivovaroff, M. J., Kaspi, V. M., Camilo, F., Gaensler, B. M., & Crawford, F. 2001, ApJ, 554, 161

Predehl, P., & Schmitt, J. H. M. M. 1995, A&A, 293, 889

Rees, M. J., & Gunn, R. E. 1974, MNRAS, 167, 1

Rodriguez, S., "Yo digo que las estrellas", from "Dias y Flores", BMG International, CD released 1975

Rybicki, G. B. & Lightman, A. P. 1979, *Radiative Processes in Astrophysics,* John Wiley & Sons, New York

Safi-Harb, S. 2002, in New Views on MICROQUASARS: the Fourth Microquasars Workshop, eds. Ph. Durouchoux, Y. Fuchs, and J. Rodriguez. Published by the Center for Space Physics: Kolkata, p. 243-252

Safi-Harb, S., & Gonzalez, M. E. 2002, in ASP Conf. Ser. 262, The High Energy Universe at Sharp Focus: *Chandra* Science, ed. E. M. Schlegel & S. B. Vrtilek (San Francisco: ASP), 315

Safi-Harb, S., Harrus, I. M., Petre, R., Pavlov, G. G., Koptsevich, A. B. & Sanwal, D. 2001, ApJ, 561, 308

Safi-Harb, S., Petre, R., Arnaud, K. A., Keohane, J. W., Borkowski, K. J., Dyer, K. K., Reynolds, S. P., & Hughes, J. P. 2000, ApJ, 545, 922

Safi-Harb, S. & Petre, R. 1999, ApJ, 512, 784

Sedov, L. I. 1959, *Similarity and Dimensional Methods in Mechanics*, Academic Press, New York

Shaver, P. A., & Goss, W. M. 1970, Australian J. Phys., Astr. Suppl., 14, 133

Shull, J. M., & van Steenburg, M. 1982, ApJ Suppl. 48, 95.

Slane, P, Gaensler, B. M., Dame, T. M., Hughes, J. P., Plucinsky, P. P., & Green, A. 1999, ApJ, 525, 357

Tanimori, T. 1998 in Proceedings of 188th IAU Symposium: The Hot Universe. ed. K. Koyama, S. Kitamoto, M. Itoh (Dordrecht: Kluwer Academic), 121

Townsley, L. K., Broos, P. S., Garmire, G. P., & Nousek, J. A. 2000, ApJ, 534, 139

Truelove, J. K. & McKee, C. F. 1999, ApJS, 120, 299

van der Hucht, K. A. 2001, NewAR, 45, 135

van der Swaluw, E. 2003, A&A, 404, 939

van der Swaluw, E., Achterberg, A., Gallant, Y. A. & Tóth, G. 2001, A&A, 380, 309

Woltjer, L. 1972, ARA&A, 10, 129

Woosley, S. E., & Weaver, T. A. 1995, ApJS, 101, 181